

# Synthetic Observations of Extremely High Velocity (EHV) SiO components in young molecular outflows

B. Vaidya<sup>1\*</sup>, T. A. Douglas<sup>1</sup>, P. Caselli<sup>1</sup>

<sup>1</sup>*School of Physics and Astronomy, University of Leeds, Leeds LS2 9JT*

23 January 2014

## ABSTRACT

A bipolar, collimated outflow is one of the first signposts of star formation. As it propagates through the molecular cloud, it injects energy and momentum via shocks and fosters chemical evolution by forming, destroying and entraining molecules along its path. High velocity molecular outflows are extensively studied for both low-mass and high-mass stars. They are usually observed using standard outflow and shocks tracers like CO and SiO. However, the exact nature of the excitation of these molecules is not yet clear due to lack of models that simultaneously study the dynamics along with complex molecular chemistry. For such a study, we have performed Magneto-hydrodynamic (MHD) simulations of knotty jet propagation into a molecular cloud using the PLUTO code. The jet dynamical quantities evolve in conjunction with different non-equilibrium cooling prescriptions of varying complexities, including molecular cooling along and H<sub>2</sub> chemistry. This prescription allows us to track the formation and destruction of HI, HII and H<sub>2</sub> along with the flow dynamics. The final state of the jet obtained for each cooling model is then given as an input to a radiative line transfer code to obtain SiO emission maps, spectra and position-velocity (PV) digrams. Our model can successfully explain the signatures of extremely high velocity (EHV) emission of SiO seen in early outflows. In particular, the line intensities, spectra and PV diagrams obtained from our model are very similar to those observed in case of outflows with EHV emission. In addition, the Atacama Large Millimeter Array (ALMA) predictions for such early molecular outflows show bright emission coming from young internal knots and bow shocks due to thermal instability. Our multi-line modeling of SiO supports the observational feature seen in Herbig-Haro (HH 211) that higher line transitions trace regions closer to the axis of the jet. The dependence of emission on different cooling prescription and abundance profiles is clearly outlined from our parameter study.

**Key words:** MHD – methods:numerical – ISM: jets and outflows

## 1 INTRODUCTION

Jets are one of the first manifestations of star formation in dense molecular cores. They are ubiquitous in both massive and low-mass star forming regions. These supersonic flows, perpendicular to the underlying accretion disk, play a vital role in removing excess angular momentum and thereby aiding in the accretion onto the protostar. For low-mass stars, they are believed to be launched by magneto-centrifugally forces and further collimated by magnetic hoop stress (Blandford & Payne 1982; Konigl & Pudritz 2000). However, in case of high-mass stars, radiative forces also contribute to flow dynamics during the later evolutionary

stages (Vaidya et al. 2011). Typically, jets are a few parsec in size and can be divided into three length-scale domains, viz. source and disk scales ( $1-10^2$  AU), envelope scales ( $10^2 - 10^5$  AU) and parent cloud scales ( $10^5 - 10^6$  AU) (e.g., Ray et al. 2007, and references therein). Of these, it is at the envelope scale where rich chemical evolution occurs as the jet interacts with the molecular medium. In this region, the jet propagates into a relatively static medium inducing shocks that are interesting from both a physical and chemical point of view. In addition to jets, molecular material from the surroundings is entrained and accelerated to high velocities giving rise to molecular outflows.

Bipolar molecular outflows from low and high-mass stars have been studied in detail over the past decade (see reviews by Bachiller 1996; Beuther et al. 2002; Arce et al.

\* E-mail: B.Vaidya@leeds.ac.uk (BV)

2007; Tafalla & Bachiller 2011). Advances in millimeter interferometers allow observations of these outflows with spatial resolution of a few arc seconds. A large number of studies observing young outflows are done using standard outflow and shock tracers, e.g. CO and SiO respectively. In addition to these molecular tracers, shocks from these outflows are detected in molecular hydrogen using infra-red telescopes. Also, energetic outflows like that of Orion source I show evidence of SiO masers very close to the launching region of a MHD disk wind (Goddi et al. 2009; Vaidya & Goddi 2013). Based on these observational studies, various empirical properties for these outflows have been discovered. For example, the high resolution interferometric studies with CO (1-0) and SiO (2-1) have revealed highly collimated jet-like outflows (with opening angles less than a few degrees); they are referred to as *molecular jets*. HH 211 is the best example of such a molecular jet (Gueth & Guilloteau 1999). Episodic knots believed to be caused by variable accretion events are a common property of young molecular outflows usually observed with higher line transitions of CO and SiO (e.g. in L1577: Gueth, Guilloteau & Bachiller 1998, in HH300: Arce & Goodman 2001a). These knots show their signatures as *wedges* in the PV diagrams (Arce & Goodman 2001b). Also, observed in these outflows are signatures of rotation and precession (e.g., in DG Tau: Bacciotti et al. 2002).

Despite this large amount of data available, the exact nature of molecular emission in outflows is not clear. For a complete understanding it is imperative to complement these observations with models. Many models based on hydro-simulations and steady state shock calculations were proposed to explain the observational signatures of molecular outflows. Among them the two main models are that of wide-angled wind driven (Shu et al. 1991) and jet driven outflow (Canto & Raga 1991). The most popular among them is the jet driven model as wind driven molecular outflows not only fail to match observed PV diagrams (Cabrit & Bertout 1992) but also tend to sweep large quantity of material at the extremities of the lobes (Masson & Chernin 1992), while the jet driven models could successfully derive the global outflow shapes and mass velocity relations of CO outflows (Raga & Cabrit 1993; Masson & Chernin 1993; Downes & Cabrit 2003, 2007). There have also been some attempts to combine these two models into one (Shang et al. 2006) to explain the global observational features. However, most of these dynamical models do not account for shock chemistry. Instead, shock chemistry is studied independently using steady state non-dissociative C-type and dissociative J-type shocks models (Neufeld & Dalgarno 1989a; Schilke et al. 1997; Flower et al. 2003). The MHD calculations by Glassgold, Mamon & Huggins (1991) suggested that molecules like SiO and CO could form within the jet. Similar conclusions of molecules surviving in steady state disk winds have also been shown (Panoglou et al. 2012). Very few simulations have modelled the outflow dynamics including molecular chemistry and in absence of magnetic fields (Raga et al. 1995; Smith & Rosen 2003). Recent models have also incorporated infall from the envelope (Rawlings, Redman & Carolan 2013) and radiation transfer (Offner et al. 2011; Offner & Arce 2013) to explain molecular emission from Class 0 protostellar outflow sources.

In the present work, our goal is to take a step further in the modeling of jet driven molecular outflows. The present model aims to consistently derive observed emission proper-

ties of molecular outflows, specifically various SiO line transitions, by combining axisymmetric MHD simulations of radiative jet propagation with time-dependent simple chemistry and 3D radiative transfer. In particular, we evolve the jet dynamical quantities in conjunction with different non-equilibrium cooling prescriptions of varying complexities. The most complex is that of molecular cooling along with hydrogen chemistry. This prescription allows us to track the formation and destruction of HI, HII and H<sub>2</sub> along with the flow dynamics. The final state of the jet obtained for each cooling model is then given as input to a non-LTE line radiative transfer code to obtain emission maps, spectra and PV diagrams. These emission maps are further processed using the Common Astronomy Software Applications package (CASA) to obtain synthetic ALMA images of the resultant molecular outflows.

In the next three sections 2, 3 and 4, we describe our numerical setup, cooling prescriptions and radiative transfer code respectively. In sections 5 and 6, we will present results from the parameter survey and the discussions along with predicted ALMA maps will be presented in sections 7 and 8, followed by conclusions in section 9.

## 2 NUMERICAL SETUP

### 2.1 Numerical code and Equations

For our study, we carry out numerical axisymmetric ideal MHD simulations using the PLUTO code (Mignone et al. 2007) which is based on a conservative scheme of Godunov type. We have modified the original code to incorporate molecular cooling from self-consistent evolution of hydrogen chemistry (see Sect. 3).

In general, the MHD code considers the following set of equations. The conservation of the mass and the momentum,

$$\frac{\partial \rho}{\partial t} + (\vec{v} \cdot \nabla) \rho + \rho \nabla \cdot \vec{v} = 0 \quad (1)$$

$$\rho \left( \frac{\partial \vec{v}}{\partial t} + (\vec{v} \cdot \nabla) \vec{v} \right) = -\nabla P + \frac{1}{4\pi} (\nabla \times \vec{B}) \times \vec{B}, \quad (2)$$

where  $\rho$  is gas density,  $\vec{v}$  the velocity vector,  $P$  the gas pressure, and  $\vec{B}$  the magnetic field vector with the poloidal and toroidal components -  $\vec{B}_p, \vec{B}_\phi$ . Note that the forces due to gravity are neglected for this problem as the domain of interest is far away from the central object.

The cooling function  $\Lambda$  which depends on temperature  $T$ , mass density  $\rho$  and chemical abundances  $\mathbf{X}$ , appears in the energy equation as a source term,

$$\frac{\partial}{\partial t} (\rho E) + \nabla \cdot \left[ \rho E \vec{v} + \left( P + \frac{B^2}{8\pi} \right) \vec{v} \right] - \vec{B} \cdot (\vec{v} \times \vec{B}) = -\Lambda(\rho, T, \mathbf{X}), \quad (3)$$

where the total energy density  $E$  of the flow comprises contributions from the internal energy  $\epsilon$ , the mechanical energy and the magnetic energy:

$$E = \epsilon + \frac{v^2}{2} + \frac{B^2}{8\pi\rho}. \quad (4)$$

The gas pressure in the flow is related to the density assuming an equation of state with the adiabatic index  $\gamma$ ,

$$P = (\gamma - 1)\rho\epsilon. \quad (5)$$

The value of  $\gamma$  is related to the degree of freedom for a mixture of gas and thus depends on the composition and temperature. We have adopted a constant value of 5/3 for the adiabatic index and have discussed the applicability for such a choice (see appendix A).

The evolution of chemical abundances for each species is solved via,

$$\frac{\partial \rho \mathbf{X}_i}{\partial t} + \nabla \cdot (\rho \mathbf{X}_i \vec{v}) = \rho \mathbf{S}_i, \quad (6)$$

where  $\mathbf{S}_i$  represents the net creation or destruction of a given species through chemical reactions (see Sect. 3).

The evolution of the magnetic field is governed by the induction equation,

$$\frac{\partial \vec{B}}{\partial t} = \nabla \times (\vec{v} \times \vec{B}). \quad (7)$$

In addition to the above set of equations, the code obeys the condition of divergence-free magnetic fields,  $\nabla \cdot \vec{B} = 0$ , which is numerically achieved by construction using the Powell's eight wave formulation (Powell et al. 1999).

## 2.2 Physical Model

We model the propagation of an axis-symmetric jet in  $(r, z, \phi)$  cylindrical co-ordinates as it interacts with the ambient medium at distances  $\gtrsim 1000$  AU. At these distances from the central source, the downward pull of gravity plays a negligible role on the dynamics of the jet. The ambient medium with which the jet interacts primarily represents the molecular cloud core. We study the interaction within a radial extent of  $20 R_{\text{jet}}$  and a vertical extent of  $100 R_{\text{jet}}$  ( $R_{\text{jet}}$  being the radius of the jet). Numerically, it is resolved by a uniform grid with a domain of  $200 \times 1000$  cells in the radial and vertical directions. For simplicity, we choose this medium to be unmagnetized and non-turbulent. The density in the ambient medium varies with vertical height  $z$  as  $\rho_{\text{amb}} \sim (\rho_0/z^2)$  which is consistent with observations at distances  $\gtrsim 1000$  AU from the center. (e.g., Keto & Caselli 2010). The value of  $\rho_0$  depends upon the density contrast,  $\eta$ , between the jet and the ambient medium. The number density in the jet is kept fixed such that the density in the ambient medium lies within a range of  $10^4 - 10^5 \text{ cm}^{-3}$ . The pressure in the ambient molecular medium is set so to maintain a constant temperature of 50 K. Note, dense molecular cores through which young outflows propagate have lower temperatures ranging from 10-20 K (Rathborne, Simon & Jackson 2007). As the jet is hypersonic in both cases, runs with lower ambient temperature of 10 K do not show any appreciable changes in final dynamical structure of the jet. Therefore, by choosing a slightly higher ambient temperature we get the same results for jet dynamics and in turn the computations are less expensive considering the large temperature gradient coupled with stiff rate equations used to model cooling in flows.

The jet enters into the medium through a nozzle of radius  $R_{\text{jet}}$  from the lower boundary ( $z = 0$ ). Optically visible jets from T-Tauri stars are just about spatially resolved for the nearest star forming regions i.e, their radii are of the order of 100 AU at a few thousand AU from the source (Ray 2012). These jets have mass outflow rates of  $\sim 10^{-7} M_{\odot} \text{ yr}^{-1}$  (Dougados et al. 2010). Younger and embedded jets in

their Class 0 phase have outflow rates about 10-100 times higher than corresponding jets from optically visible young stars (Bally 2007; Dionatos et al. 2009; Ray 2012). Also, these optically obscure jets are relatively slower with velocities ranging around  $100 \text{ km s}^{-1}$  (Bally 2007) as compared to optically visible flows with velocities up to  $500 \text{ km s}^{-1}$  (e.g, Mundt, Brugel & Buehrke 1987). For the present model, the jet is injected into the domain with a velocity of  $v_{\text{jet},0} = 100 \text{ km/s}$  and the jet density is set to  $10^5 \text{ cm}^{-3}$  within a jet radius of  $2.5 \times 10^{15} \text{ cm}$ . Outside this radius, the physical quantities are fixed to their ambient values. With these choices, we obtain a mass outflow rate of  $10^{-6} M_{\odot} \text{ yr}^{-1}$ , consistent with young jets. Most of the young outflows show variable features possibly due to variable accretion rates or internal shocks inside the jet (e.g. Bachiller 1996). We replicate such variability by superimposing the constant jet velocity with sinusoidal pulsation with an amplitude of  $25 \text{ km s}^{-1}$  with a periodicity of 70 yr such that the dense knots are separated by a distance of  $\sim 1000$  AU.

Thermal and magnetic properties of jets from young stars are difficult to constraint because of their large variation not only within the jet but also in its surroundings. Forbidden line emissions from HH objects indicate excitation temperatures of the order of  $\leq 10^4$  K (Podio et al. 2006; Bally 2007). However, in case of young jets, the temperature is considerably lower (i.e, by an order of magnitude) than found in jets from Class I/II sources as derived from various atomic lines in molecular jets from L-1448C and HH211 (Dionatos et al. 2009, 2010). The temperature at the jet nozzle for our model has been set to 1000 K to be consistent with values obtained for young jets. Thus, the jet is over-pressured by 60 times as compared with the ambient medium, assuming  $\eta = 3.0$ . Inside the jet beam, a radial variation of thermal and magnetic pressure is adopted to maintain a magneto-static equilibrium for all our runs (Stone & Hardee 2000). Based on these profiles, the toroidal magnetic field is assumed to be zero at the axis and achieves a maximum at radius,  $r_m \sim 0.8 R_{\text{jet}}$  inside the jet. Though measuring magnetic fields in most jets is not possible via unpolarized nebular lines, in some special cases like HH 34S and HH 111V, it has been measured to be 10 and  $30 \mu G$  respectively (Morse et al. 1993). Considering the dependence of such weak magnetic fields on density and radial distance in velocity-variable flows, Hartigan et al. (2007) have shown that at large distances from the star these fields only play a minor role in the dynamics. Thus, for all our runs the value of magnetic field strength,  $B_{\phi}(r_m)$  is set to be  $\sim 37 \mu G$ .

In order to consistently model the SiO emission arising from shocks as this jet interacts with the medium, we evolve the dynamics along with chemistry and cooling prescriptions. They are described in details in the next section.

## 3 CHEMISTRY AND COOLING

### 3.1 Molecular Chemistry

Typically, young collimated outflows have cooling times shorter than the dynamical times, implying that the radiative cooling plays a vital role in their dynamics. In order to study such outflows it is necessary to evolve the dynamics in conjunction with full molecular chemistry and associated radiative processes. However, evolving a full complex network

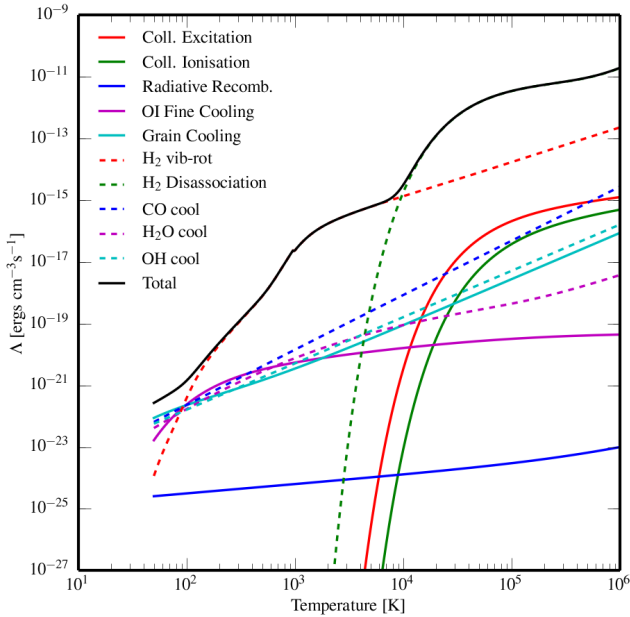


**Figure 1.** Variation of the cooling function  $\Lambda(n, T, \mathbf{X})$  with temperature for the initial state.

of chemical equations along with dynamics is a very computationally intensive task. As a result, we have focused only in evolving the chemical equations pertaining to atomic and molecular hydrogen. This prescription of molecular cooling has been added to the PLUTO code to study the chemical evolution of molecular outflows during the very early phases of star formation. In particular, the total hydrogen number density  $n_{\text{H}}$  comprises of contribution from atomic and molecular hydrogen i.e.,  $n_{\text{H}} = n_{\text{HI}} + n_{\text{H}_2}$ . Whereas the contribution to electrons comes from the ionized hydrogen,  $n_{\text{HII}}$  and from negligible but fixed fraction of metals ( $Z \sim 10^{-4}$ ). Numerically, the non-homogenous parts of the equations 3 and 6 are solved separately from the advection step using operator splitting. Further, the rate equations are evolved at each advection time step using sub-stepping and adaptive Runge-Kutta methods. The formation and destruction of fractions (denoted by  $\mathbf{X}_i$  in eq. 6) of three species, viz.,  $\text{fHI}$ ,  $\text{fH}_2$  and  $\text{fHII}$  are tracked by the code based on the temperature dependent reaction rates whose coefficients are specified in Table 1 along with their literature references.

### 3.2 Cooling Prescriptions

Figure 1 shows the variation of the cooling function,  $\Lambda(\rho, T, \mathbf{X})$ , with gas temperature assuming conditions of initial ambient density. Various processes that contribute to the cooling function in our model are listed in the figure. The formulations of these contributions are adopted from (Smith & Rosen 2003; O’Sullivan & Camenzind 2009, and references therein). For low temperatures, we also take into account contributions to the cooling function from molecules like CO, whose abundance with respect to  $n_{\text{H}}$  is fixed to a value of  $10^{-5}$  assuming an average CO depletion factor across the envelope of  $\sim 10$  (e.g. Crapsi et al. 2005). For each of the other molecules contributing to the cooling function (like OH,  $\text{H}_2\text{O}$  and atomic OI) the abundance is fixed

to values of  $5 \times 10^{-6}$ . Note, the uncertain abundance values are rather arbitrary for these molecules. For example, the adopted abundance of  $\text{H}_2\text{O}$  is higher than that found by Caselli et al. 2012 in a pre-stellar core ( $\lesssim 10^{-7}$ ). In spite of such over estimated abundance values, their contribution is only important when temperature is  $< 100$  K as seen in figure 1. As the internal shocks, where most of the molecular hydrogen is produced, maintain temperatures higher than 100 K and densities  $\sim 10^6 \text{ cm}^{-3}$ , cooling due to these molecules do not play a significant role even if the arbitrary abundance is increased by a factor of 10 (Smith & Rosen 2003). Instead, a substantial contribution to the cooling function, between  $T = 100$  K and 3000 K, comes from the vibrational and rotational transitions of molecular hydrogen during the initial stages of jet evolution. For temperatures above 3000 K the cooling is mainly via  $\text{H}_2$ . The total curve for the whole temperature range obtained in our runs is shown in black. The fact that the initial ambient medium is largely molecular, cooling is also dominated by molecular processes. In our reference model (see 5.2), we update this curve at each time step based on the fraction of various hydrogen species. Thus, during the evolution, contributions from collisional ionizations and excitations become important in regions dominated by atomic and ionized hydrogen.

We also ran simulations of axi-symmetric MHD jets with optically thin cooling prescriptions already existing in the public release of the PLUTO-4 code. They are power-law cooling, simplified non-equilibrium (or atomic) cooling (Teşileanu, Mignone & Massaglia 2008) and tabulated cooling. While these additional cooling prescriptions may not be a complete description of the chemical and radiative processes in early outflows, they are ideal to compare the results obtained from the more consistent newly added molecular cooling. In addition, we compare these radiative runs with an adiabatic jet to cover a wide spectrum of jet thermodynamics. Such a comparison is presented in section 6.1.

## 4 RADIATIVE TRANSFER

### 4.1 The radiative transfer code

The radiative transfer program used is LIME (Line Modeling Engine; Brinch & Hogerheijde 2010), which calculates line intensities based on a weighted sample of randomly chosen points in a continuous 3D model. The method of selecting these points is given in section 4.2. At each of these points, the density of the main collision partner (equivalent amount of H, given by  $n(\text{H}_2) + n(\text{HI})$ , assuming that ionized Hydrogen does not collide with SiO), gas temperature, velocity, molecular abundances and turbulent velocity are specified. These points are then smoothed by Lloyd’s algorithm (Lloyd 1982) in order to minimise the variation in distance between points whilst keeping the same underlying distribution. These points are then connected by Delaunay triangulation and it is between the points connected by this method that photon are allowed to propagate (fig. 2). The level populations of the selected molecules are calculated at each of these points from collisional and radiative (de)excitation and the local radiation field is calculated. This is repeated 20 times with the populations of each level converging towards a single value. This number of iterations



**Table 1.** Summary of the chemistry reaction set. T is the temperature in Kelvin,  $T_{\text{eV}}$  is the temperature in electron-volts,  $T_5 = T/1 \times 10^5$  and  $T_2 = T/100$

No.	Reaction	Rate Coefficient ( $\text{cm}^3\text{s}^{-1}$ )	Reference <sup>a</sup>
1.	$\text{H} + \text{e}^- \rightarrow \text{H}^+ + 2\text{e}^-$	$k_1 = 5.85 \times 10^{-11} T^{0.5} \exp(-157,809.1/T)/(1.0 + T_5^{0.5})$	1
2.	$\text{H}^+ + \text{e}^- \rightarrow \text{H} + \text{h}\nu$	$k_2 = 3.5 \times 10^{-12} (T/300.0)^{-0.8}$	2
3.	$\text{H}_2 + \text{e}^- \rightarrow 2\text{H} + \text{e}^-$	$k_3 = 4.4 \times 10^{-10} T^{0.35} \exp(-102,000.0/T)$	3
4.	$\text{H}_2 + \text{H} \rightarrow 3\text{H}$	$k_4 = 1.067 \times 10^{-10} T_{\text{eV}}^{2.012} \exp(-(4.463/T_{\text{eV}})(1. + 0.2472T_{\text{eV}})^{3.512})$	4
5.	$\text{H}_2 + \text{H}_2 \rightarrow \text{H}_2 + 2\text{H}$	$k_5 = 1.0 \times 10^{-8} \exp(-84,100/T)$	2
6.	$\text{H} + \text{H} \xrightarrow{\text{dust}} \text{H}_2$	$k_6 = 3.0 \times 10^{-17} \sqrt{T_2}(1.0 + 0.4\sqrt{T_2 + 0.15} + 0.2T_2 + 0.8T_2^2)$	5

<sup>a</sup> REFERENCES – (1) Cen (1992) [Eq. 26a]; (2) Woodall et al. (2007) [UMIST Database] (3) Galli & Palla (1998) [Eq. H17]; (4) Abel et al. (1997) [Tab. 3 Eq. 13]; (5) Hollenbach & McKee (1979) [Eq. 3.8]

is sufficient for the signal to noise ratio of the level populations (as defined in Brinch & Hogerheijde 2010) to exceed 1000 for 99% of the points, ensuring that the simulation has converged on a stable level population. After 20 iterations the model is ray-traced in order to produce synthetic brightness maps. The average of ten separate runs was taken to minimise the artefacts in the output images, resulting from the grid construction.

#### 4.2 Grid construction

In order to construct the grid, candidate points are randomly selected from the volume to be simulated. These candidates then have their equivalent  $\text{H}_2$  number density, and the number density of SiO, compared against those of a reference point in order to decide if the candidate point is to be used in the grid or not. Candidate grid points are selected at random in a cylindrical coordinate system that is linearly spaced in  $z$  and  $\theta$  and logarithmically spaced in  $r$ . For each point to be selected, a random number  $\alpha$  is drawn from the semi-open set  $[0, 1)$  as a threshold. After selection of random coordinates, the  $\text{H}_2$  number density and SiO number density at the candidate point ( $n$  and  $m$ , respectively) are compared against the number densities of a reference point in the unperturbed ambient medium multiplied by a factor of  $\frac{4\eta}{5}$  ( $n_{\text{ref}}$  and  $m_{\text{ref}}$ ), where  $\eta$  is the density contrast between the jet and ambient medium. If  $\alpha < \left(\frac{n}{n_0}\right)^{0.3}$  or  $\alpha < \left(\frac{m}{m_0}\right)^{0.3}$  then the point is selected for use. Otherwise another  $r$ ,  $\theta$ ,  $z$  co-ordinate is selected and it becomes the candidate point. In addition to this method of selection, 5% of the points are linearly distributed in  $x$ ,  $y$  and  $z$  with no bias with regards to density or abundance. This provides a minimum level of sampling for the large low density regions in the outer parts of the simulated volume.

#### 4.3 SiO abundance

Molecular abundance is one of the important ingredients that is required by the radiative transfer code described above. Typically, extremely low abundance of SiO is found ( $n(\text{SiO})/n(\text{H}_2) < 3 \times 10^{-12}$ ) in dark, dense clouds such as TMC1 (Ziurys, Friberg & Irvine 1989; Martin-Pintado, Bachiller & Fuente 1992). Whereas in outflows like L1448, SiO abundance can increase up to  $10^{-6}$  (Martin-Pintado,

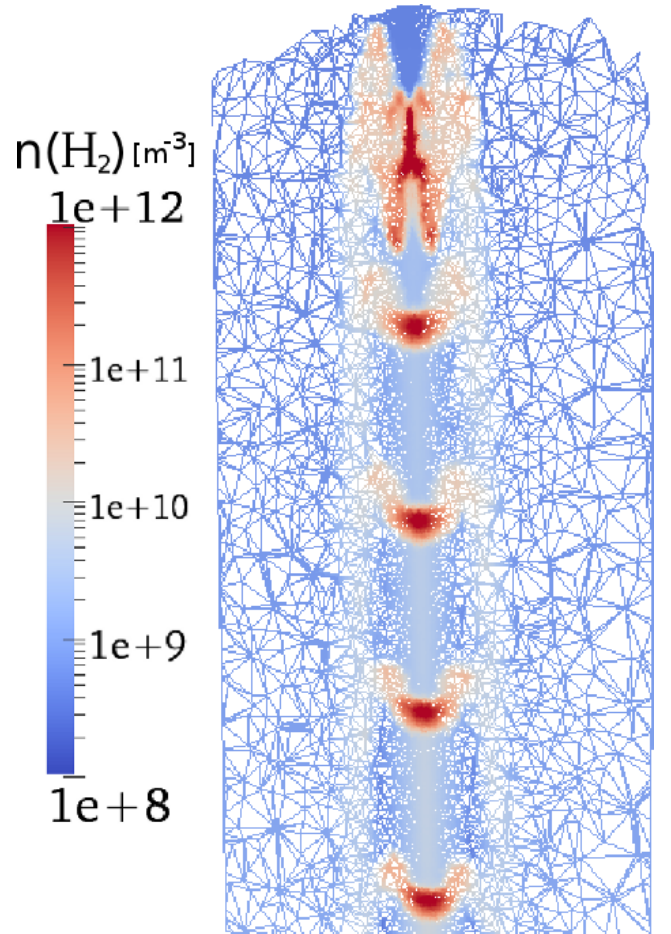


**Figure 2.** A plot of the points selected by the gridding process and the paths down which photons can propagate for points in the  $r, z$  plane. The points are color coded by the density distribution (in  $\text{m}^{-3}$ , as used in LIME) and are more concentrated in the high density knots.

Bachiller & Fuente 1992; Dutrey, Guilloteau & Bachiller 1997). Thus, there is an increase of 6 orders of magnitude from quiescent clouds to outflows. Production of gaseous SiO due to slow C-type shocks has been suggested to occur via release of silicon from grain cores and to a lesser extent from grain mantles. Various stationary shock models indicate a sudden abundance increase in SiO near a shock speed

of 20-30 km s<sup>-1</sup>. However, several young outflows have velocities of the order of 100 km s<sup>-1</sup> as in the present case. In L1448, [Martin-Pintado, Bachiller & Fuente \(1992\)](#) have shown that for extreme velocities (obtained from shift in the spectra) of -40 to -50 km s<sup>-1</sup>, the SiO abundance could be as large as  $6 \times 10^{-7}$ , while, it slightly increases to  $2 \times 10^{-6}$  for the velocity range of -60 to -50 km s<sup>-1</sup>. For the same source, typical working surface velocities of the *molecular bullets* are estimated to lie around 60-175 km s<sup>-1</sup> [Dutrey, Guilloteau & Bachiller \(1997\)](#). Shocks due to such outflows could dissociate H<sub>2</sub>, and molecules observed in such energetic outflows could have been reformed in the post-shock gas as suggested by detailed models of J-shocks by [Neufeld & Dalgarno \(1989b\)](#). SiO formation in J-shocks has also been modelled recently and has thought to be the source of the SiO line emission observed in molecular outflows and jets ([Guillet, Jones & Pineau Des Forêts 2009](#)).

The velocities obtained from the dynamical simulations are the jet flow velocities. They can well be different from the shock velocities depending upon the density contrast between the jet and ambient medium. For the bow shock, one can estimate the shock velocity by equating the pressures across the shock surface (e.g., [Masson & Chernin 1992](#)):

$$v_s = \frac{v_{\text{jet}}}{1 + \eta^{-0.5}} \quad (8)$$

where  $v_s$  is the velocity of the bow shock and  $v_{\text{jet}}$  is the jet velocity. Considering the dependence of ambient density on the vertical distance, the density contrast at the bow shock increases to  $\eta \sim 100$ . Thus, for such large  $\eta$  values, one can very well approximate the bow shock velocity to be the same as the jet flow velocity. In case of internal knots, the above equation for the velocity of the working surface changes to eq. B2 ([Raga & Kofman 1992](#)). As described in the appendix B, the velocity of the internal knots effectively reduces to an average of upstream and downstream velocities across the knot and can as well be approximated to be the same as the flow velocity. However, the shock velocity in the frame of reference of the knot can be considerably different than the flow velocity and is expressed as a difference between the upstream and downstream velocities. In the present models, these internal shock velocities are  $\leq 20$  km s<sup>-1</sup>. Steady state calculations of shocked grain micro-physics described above, takes into account these internal shock velocities to estimate SiO abundances. On the other hand, molecular lines provide information about the bulk velocity of the flow.

In spite of all numerical models relating to the study of enhancement of SiO in shocks, very little is known about the dependence of SiO abundance on shock speeds. Considering the complex grain chemistry that is involved in order to estimate the functional dependence of SiO abundance on shock speeds, we prescribe these profiles based on limited empirical evidences and approximate the variation of SiO abundances on jet flow velocities. The most simple and extreme choice among them is the step profile in which the SiO abundance is a low value of  $10^{-12}$  below 20 km s<sup>-1</sup> and a maximum value of  $10^{-6}$  beyond. Such a choice effectively reduces to assuming a constant value of high abundance for the flow velocities seen in our model. In order to compare such a choice, we also apply a top-hat profile where above 100 km s<sup>-1</sup>, abundance value is set again to a low value of  $10^{-12}$ . With such extreme choices we are over-estimating the abundance values in the

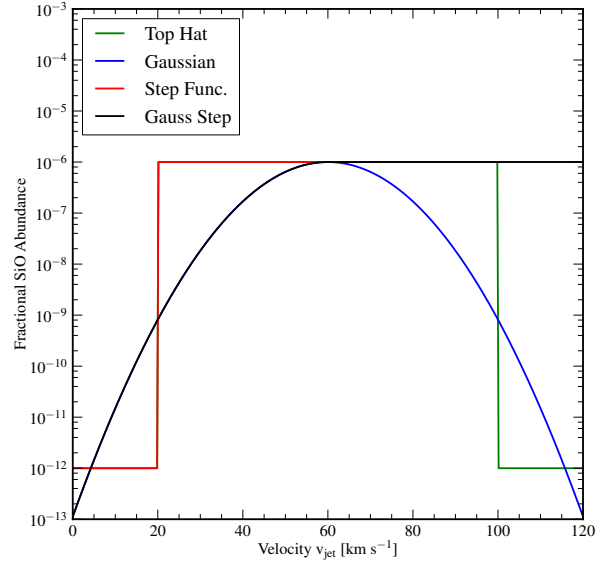


**Figure 3.** The different fractional SiO abundances as a function of jet velocity,  $v_{\text{jet}}$ .

jet interface, however, in regions close to internal knots, the abundance values will be within a factor of 2. In order to get rid of an arbitrary discontinuous change of abundance, we also prescribe a Gaussian such that the peak SiO abundance of  $10^{-6}$  is at 60 km s<sup>-1</sup>, while the value of  $n(\text{SiO})/n(\text{H}_2)$  falls below  $10^{-9}$  at 20 and 100 km s<sup>-1</sup>. Such a huge variation in SiO abundance may indeed be the case in regions where SiO is seen widespread (e.g., [Lefloch et al. 1998](#), also see section 8). Also along with a Gaussian profile, we consider the case where we consider an abundance of  $10^{-6}$  beyond 60 km s<sup>-1</sup>. In addition to this, if the temperature at the point is greater than 92,000 K (the temperature of the Si-O bond disassociation energy) the abundance is reduced to 0. These functional dependence of SiO abundance on jet flow velocities are shown in figure 3 and a comparative view is further discussed in Sec 6.4.

## 5 PARAMETER SURVEY

The results and analysis for the present work are divided in two parts: the dynamical numerical simulations and the radiative transfer analysis. For each part we have used certain parameters and the effect of changing them is studied. Ideally all these parameters should come from observational results. However, not all quantities needed for our study are well constrained by observations, thus they are considered as free parameters. Such a parameter survey provides better handle on the range of allowed values on qualitative comparison with observations.

### 5.1 Parameter definitions

For the first part of the study concerning the dynamical numerical simulations, we will focus on two main parameters. They are the prescription of cooling and the density

contrast between the jet and the ambient medium denoted by  $\eta$ . The various cooling prescriptions used for the present study are described in detail in section 3. They differ in the physical process that is responsible for cooling and chemistry. The most simple one is that of power-law cooling with no chemistry and the most complex cooling module is where molecular hydrogen chemistry is evolved with contributions to cooling from other abundant molecules like CO, OH etc.

A value of  $\eta > 1$ , means that that jet is over dense with respect to the medium. In all our runs with different cooling prescriptions, we have assumed the jet to be over-dense by 10 times compared to the ambient medium. Additionally, for the atomic, tabulated and molecular cooling runs (see section 3 for description of different cooling prescriptions) we have also used a value of  $\eta$  of the order of unity indicating similar densities in the jet and the medium. Table 2 lists all the runs with varying  $\eta$  and cooling prescriptions, along with the peak intensity and line widths of SiO(2-1) at the bow shock.

To obtain the SiO emission maps and corresponding spectra, two additional free parameters are required along with other inputs described in section 4. They are the fractional abundance profile of SiO and the angle of inclination with respect to line of sight denoted by  $i$ . Section 4.3 describes all the profiles used for the present study.  $i = 90^\circ$  indicates that the outflow is in the plane of the sky. Additionally, we have used two other angles of inclination apart from the plane of the sky, i.e.,  $i = 45^\circ, 60^\circ$  to compare results with observations. The runs with different fractional abundance profiles are described in section 6.4

## 5.2 Reference Run

We define a reference run in order to quantify and compare results obtained from such a survey of above mentioned parameters. The results shown in this work will be pertaining to the reference run (unless otherwise mentioned) and appropriate comparison will be discussed with other runs.

The reference run in our calculation has density contrast  $\eta = 3$  with the initial jet density of  $10^5 \text{ cm}^{-3}$ . This jet enters the ambient medium with a velocity of  $v_{\text{jet},0} = 100 \text{ km s}^{-1}$ , which is further superimposed by sinusoidal perturbations to replicate dense knots. The maximum value of toroidal magnetic field is set to be  $37 \mu\text{G}$  at the base of the jet. Dionatos et al. (2009) have detected atomic lines towards a molecular jet from L1448-C, indicating a presence of an embedded atomic jet. Additionally, they also detect pure rotational transitions from  $\text{H}_2$  indicating the presence of molecules along with the atomic jet. Line ratios from this source indicate that the atomic gas is characterized by an ionization fraction of 1%, which is considerably less than as compared to ionization fraction of 10-20% measured in optical jets (Bacciotti, Chiuderi & Oliva 1995). Initial jet composition is prescribed to be 89% atomic, 10% molecular and 1% ionized, in qualitative agreement with above observational results.

The cooling in the reference jet is via molecular cooling prescription, whereby the initial hydrogen fractions are evolved using appropriate rate equations and with cooling contributions for abundant molecules like CO, OH etc. The final state (at time  $\sim 1000 \text{ yr}$ ), i.e., density, temperature and velocity obtained from this run are given as inputs to the

radiative transfer code to obtain the observational features corresponding to SiO molecules. For the radiative transfer calculation, the source in the reference run is stationary and the jet is in the plane of the sky ( $i = 90^\circ$ ). A Gauss Step (see fig 3) is used for the fractional abundance of SiO.

## 6 RESULTS

### 6.1 Comparison of cooling prescription

We have done a comparison study of jet dynamics with various cooling prescriptions, which are described in Sect. 3. Figure 4 shows the volume density of the MHD jet at time  $\sim 1000$  years for these different cooling prescriptions. For this study, we have chosen a density contrast at the base of  $\eta = 10$  between the jet and ambient medium. It is clear from the figure 4, that the cooling plays a significant role in determining the structure of the jet. The jets with no or very little cooling are much wider compared to jets having dominant cooling. For example, the adiabatic jet has the widest bow shock at its apex and has the most prominent shell of processed material, also known as the cocoon, around it. While the jet with atomic cooling has a rather conical jet head with significantly less cocoon surrounding it. The cocoon is almost absent from the narrow jet with tabulated cooling. Instead, the jet seems to form a very high density shell due to cooling of the processed ambient gas. Further, the jet with tabulated cooling is narrower than the jet with molecular cooling. This clearly shows the feedback of chemistry on the cooling function. The cooling terms for both these jets are the same to begin with, however, for the molecular jet the cooling terms evolve with jet dynamics as the fraction of various hydrogen species change over time. On the contrary, the terms remain fixed to the initial values, shown in fig 1, for the jet with tabulated cooling. Additionally, the material at the bow shock for the jet with tabulated and molecular cooling condenses forming dense knots. Such a condensation is due to thermal instability and is a typical feature of axi-symmetric radiative jets (see, for e.g, Blondin, Fryxell & Konigl 1990; Cerqueira & de Gouveia dal Pino 1999).

The dynamical states for each of this cooling prescriptions are then given as inputs to the radiative transfer code to obtain integrated SiO(2-1) emission maps shown in figure 5. The differences in dynamical features are also reflected in the corresponding SiO emission maps. These maps are obtained assuming an angle of inclination of  $90^\circ$  using the top hat abundance profile. They are then placed at a distance of  $16.7 \text{ pc}$  and convolved with a beam with FWHM of  $2.0''$  in order to create the maps shown. The emission from the jet with atomic cooling is coming from the conical jet head and younger knots closer to base of the flow. Additionally, features in the shell at  $Z/R_{\text{jet}} \sim 60, 75$  also show evidence of faint emission. In case of the jet with power-law cooling, the emission mostly arises from the internal knots. The emission coming from jets with tabulated and molecular cooling resembles that observed in young molecular outflows, although the tabulated jet is narrower. Also in these outflows, strong emission arises from the condensation formed at the bow shock due to thermal instability.

In summary, different cooling prescriptions strongly influence the dynamics of MHD jet propagation, in particular

**Table 2.** Summary of parameter runs for different cooling prescriptions and density contrasts. Integrated emission map for SiO(2-1) line in units of  $\text{K-km s}^{-1}$  obtained by convolving with a beam of  $15''$  and the corresponding line widths (in units of  $\text{km s}^{-1}$ ) are listed for each of these runs for two different abundance profiles.

Run	Cooling Mode	$\eta$	Top Hat Profile		Gaussian Profile	
			$\int TdV$ [ $\text{K-km s}^{-1}$ ]	$\Delta v$ [ $\text{km s}^{-1}$ ]	$\int TdV$ [ $\text{K-km s}^{-1}$ ]	$\Delta v$ [ $\text{km s}^{-1}$ ]
adi10	Nil (Adiabatic)	10	2.91	>40	0.25	40.0
pow10	Power law	10	0.64	8.0	0.02	10.0
atm10	Atomic	10	2.04	36.0	0.58	38.0
atm2	Atomic	2	3.21	18.0	0.64	20.0
tab10	Tabulated	10	0.75	11.0	0.09	10.0
tab2	Tabulated	2	2.89	8.0	1.0	9.0
mol10	Molecular	10	1.10	10.0	0.1	11.0
mol3	Molecular	3	3.3	14.0	0.66	12.0

the thickness and structure of the bow shock. These dynamical differences are also reflected in SiO emission maps. The molecular cooling in our model consistently takes into account the feedback of temperature and density variation to evolve the chemical species, unlike the tabulated cooling where the fraction of chemical species remains fixed. Thus, for our reference run we will adopt the molecular cooling prescription and compare results with observations. The properties of molecular cooling flows are described in details in the next section.

## 6.2 Molecular cooling and $\text{H}_2$ chemistry

The molecular cooling in our model takes into account the evolution of  $\text{H}_2$  chemistry along with contributions to cooling from fixed fractions of other molecules like CO, OH etc. Figure 6 shows the color composite image of various hydrogen fractions, (fHI (red), fH<sub>2</sub> (green) and fHII (blue)), from the dynamical simulation with reference parameters. The jet beam is largely dominated by atomic hydrogen, while molecular hydrogen is seen to be formed in internal knots and region that is thermally in-stable. Ionized hydrogen is mainly formed at the tip of the bow. The highest temperature of  $\sim 50000$  K is attained in our flow at the tip of the bow shock. While the temperature on the edges (i.e., the interface between jet and the ambient medium) is lower than 5000 K. Also, the relatively weaker shocks formed nearby knots do not heat up the material beyond  $10^3$  K.

The distribution of fractions of different hydrogen species along with temperature suggests that there are essentially three regions where chemistry is evolved due to shocks. They are : (1) the tip of the jet , (2) the edges of the jet and (3) intermediate knots. As the atomic jet propagates from the lower boundary into the cold molecular medium , it forms a strong shock resulting in a density and temperature discontinuity. Such a jump in dynamical quantities plays a crucial role in the evolution of chemistry. For example, temperatures beyond few 1000 K produced in the shocks could disassociate the molecules and can also lead to ionization if the temperature becomes larger than  $10^4$  K.

For the reference run, the effect of the shock in the dynamical evolution of the hydrogen fraction is presented in figure 7. The top panel of the figure shows the hydrogen number density in the jet. The fraction of all hydrogen forms are shown in the bottom panels of figure 7 along two rep-

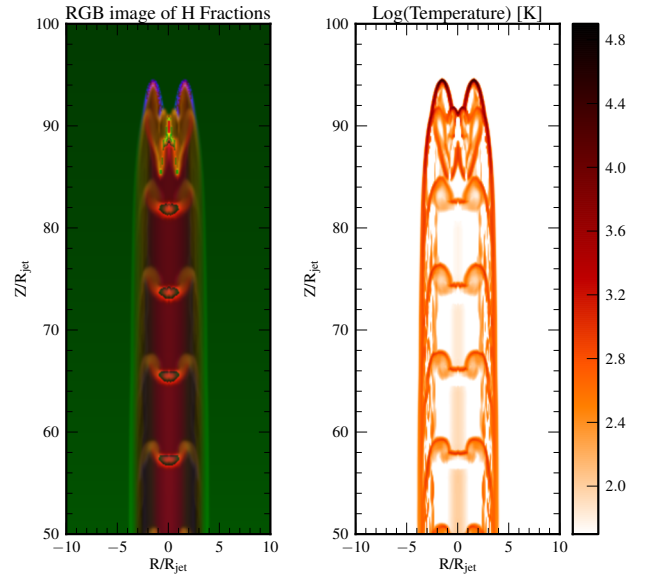


**Figure 6.** *Left:* Color composite image of various hydrogen fractions, fHI (red), fH<sub>2</sub> (green) and fHII (blue), for the reference run. For better visualisation, the ionized hydrogen fraction is enhanced by a factor of 100. The temperature of the jet obtained from dynamical simulation is shown on the *right*.

resentative regions in the jet marked with the arrows. The left bottom panel shows the vertical distribution of temperature, molecular and atomic fraction at the interface of the knot and the ambient medium. The interaction of the knot with the medium raises the temperature to 1000 K and accumulates matter so that the density increases up to  $10^6 \text{ cm}^{-3}$ . Behind the shock as the material cools, atoms combine together to form molecules as seen in the increase of fH<sub>2</sub> from 0.44 to 0.52. Further away from the shock, atomic and molecular hydrogen tend to reach a quasi equilibrium as their fractions reach a value of 0.5. The ionized fraction is extremely low ( $< 10^{-3}$ ) in this region due to the low temperatures. However at the bow-shock, temperatures rise up to 20000 K. Molecular hydrogen species are destroyed, while ionized hydrogen shows an increase in its fraction (figure 7, bottom right panel). The peak in ionized fraction of 0.15



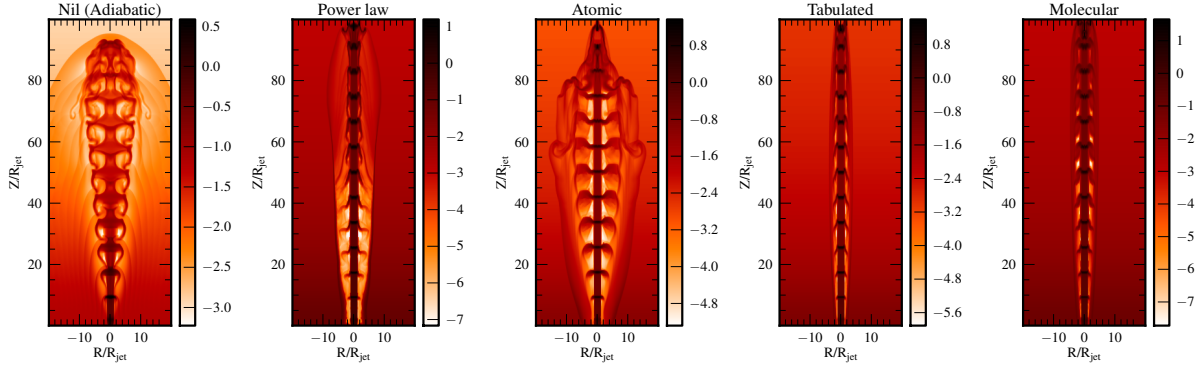


**Figure 4.** Logarithmic values of jet volume density in units of  $\text{cm}^{-3}$  obtained from dynamical simulations for different cooling modes (labelled on the top of each panel) with  $\eta = 10$ .

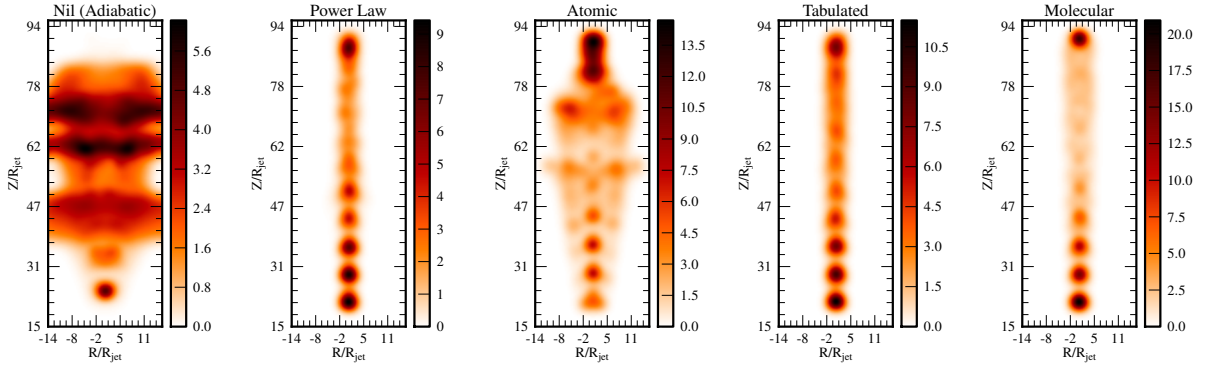


**Figure 5.** A plot of the integrated SiO(2-1) emission from 5 models in units of  $\text{K-km s}^{-1}$ , each using a different method to calculate cooling (labelled on the top of each panel) and all with  $\eta=10$ .

coincides with the peak in temperature profile as expected. The molecular fraction shows a considerable dip from 0.3 to 0.03 at this temperature before rising sharply in the ambient molecular medium.

### 6.3 Emission maps, spectra and PV diagrams

The output obtained from the radiative transfer calculation is a data cube with velocity being the third axis. This allows us to obtain spectra and position velocity diagrams from these data cubes. Figure 8 shows outputs from the data cube for SiO(2-1) in the reference run. The top left panel in the figure shows the emission map for the jet. The notable features are the knots close to the base of the jet and the emission near the bow shock due to density enhancement by cooling instability. The PV diagram shown in the top right panel is obtained along the jet as indicated by the vertical magenta line in the left panel. The velocities are shown in the X-axis. High velocity features are clearly seen in regions corresponding to the knots in the emission maps. These features fade along the jet as the knots also disappear in the emission map. The region close to the bow shock also shows high velocity features.

The spectra at three different positions in the flow are shown in the bottom panel of figure 8 (they are marked with green crosses in top left panel). The knot closer to the base and the region near the bow shock shows a peak

intensity of 15-20 K. Whereas, the intensity decreases and reaches about 5 K in the middle of the jet. The line widths seen are typically around  $5\text{--}10 \text{ km s}^{-1}$ . These line widths increase substantially as the angle of inclination decreases. Figure 9 show the emission map, PV diagram and spectra for the same reference run but with angle of inclination of  $45^\circ$  respectively. The line widths now are typically of the order of  $20 \text{ km s}^{-1}$ . The PV diagrams in these runs are no longer symmetric. Instead, they show a distinct *zig-zag* pattern at each of the knots and region close to the bow shock.

### 6.4 SiO Abundance profile

The fractional abundance of SiO has been assumed to vary with jet flow velocity in a simplistic manner (see sec 4.3). In figure 10, we compare the maps for SiO(2-1) emission at an inclination angle of  $90^\circ$  for four different abundance profiles. There is a striking difference with regards to emission from the internal knots in these images. Using the step profile results in emission from all the internal knots in the SiO(2-1) line. However, some of the knots are not observed when using the top-hat profile. Similar qualitative characteristics are seen in case of a Gaussian abundance profile. In particular, the case where abundance decreases smoothly beyond  $60 \text{ km s}^{-1}$ , produces emission only from the region closest to the bow shock and the lower most knot, while the internal knots do not show any appreciable emission. While,

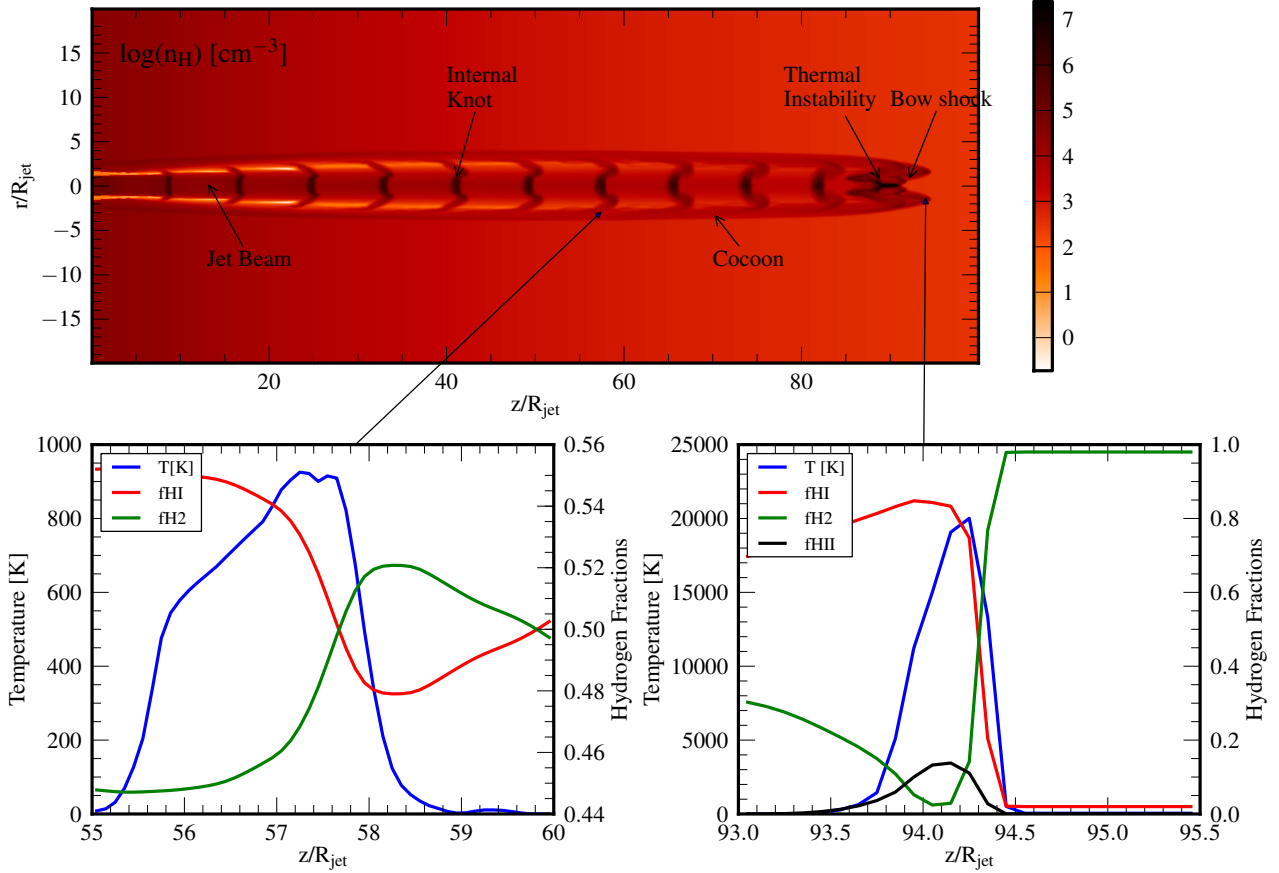


**Figure 7.** *Top:* Logarithmic values of total hydrogen number density,  $n_{\text{H}}$ , in units of  $\text{cm}^{-3}$ , obtained from the reference run along with labels of typical jet features. *Bottom:* Dependence of hydrogen fractions on the temperature at two points in the flow, viz. at the interface of the knot (*left*) with molecular medium and at the bow shock (*right*).

the Gauss Step profile produces very similar features as that of the step profile effectively making the initial rising part of the curve unimportant.

The dependence of emission on SiO abundance profile is expected due to the distribution of jet velocities obtained from the dynamical simulations. We see that the velocity of internal knots lie around  $80\text{--}90 \text{ km s}^{-1}$ , as the pulsed jet was injected with a mean of  $100 \text{ km s}^{-1}$ . The knots slow down during the evolutionary phase as they interact with the ambient medium. Interestingly, younger knots closer to the base of the jet are brighter compared to older ones further away from the jet (see panels 1 and 3 of fig 10). This is attributed to the fact that the ambient medium has a density gradient that goes as  $\sim z^{-2}$ . Thus, the younger knots suffer the most deceleration closer to the base of flow. This process is further validated by the decreasing abundance profile giving rise to lack of emission from internal knots in panel 3 of the fig 10.

Additionally, the internal knots show their distinct signatures in form of *wedges* as seen in the PV diagrams for these different profiles (see 6.3). Figure 11 shows a zoomed in version of the bottom four internal knots in form of a PV diagram for these different abundance profiles. As expected, the signatures of knots is missing for the case with Gaussian profile without a step. Further, the wedges formed in panels 1, 2 and 4 of the figure in general are slightly more extended

as compared to those formed in panel 3. This is indeed because of the discontinuous nature of the top-hat abundance profile as the SiO is enhanced to a maximum abundance for all velocities between  $20$  and  $100 \text{ km s}^{-1}$ , which is not the case in a more continuous Gaussian distribution.

## 7 ALMA VIEW

In order to see the interior structure of the molecular outflow and test the model predictions, high resolution interferometric observations are needed. We have performed synthetic Atacama Large Millimeter Array (ALMA) observations using the Common Astronomy Software Applications package (CASA). The output from the radiative transfer were scaled to a distance of  $300 \text{ pc}$  and used as the sky models for observations of the  $J=2-1$ ,  $J=5-4$  and  $J=8-7$  lines of SiO at frequencies of  $86.85$ ,  $217.10$  and  $347.33 \text{ GHz}$ , which fall in ALMA bands 3, 6 and 7, respectively. The observations were simulated using cycle 2 ALMA for 25 minutes total integration time, in the configurations c32-6, c32-4 and c32-3 for the three lines, giving beam sizes of  $0.72''$ ,  $0.47''$  and  $0.58''$  and sensitivities of  $0.05$ ,  $0.07$  and  $0.09 \text{ mJy/beam}$  for the three lines (as calculated by the ALMA online sensitivity calculator) with velocity resolutions of  $\sim 1 \text{ km/s}$ . Figure 12 presents the ALMA prediction obtained from our reference

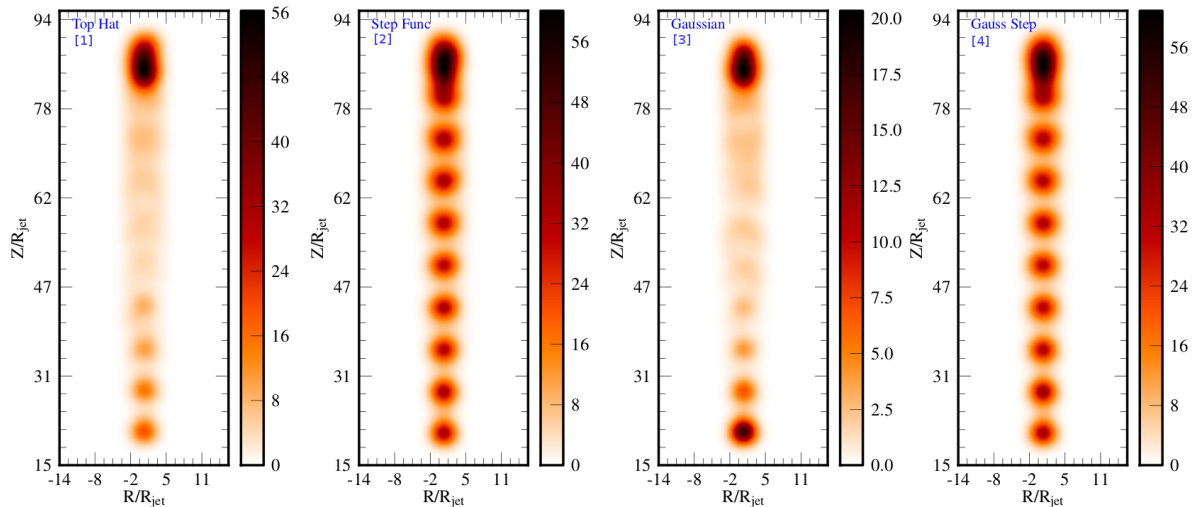


**Figure 10.** Integrated intensity maps of SiO(2-1) line in units of  $\text{K-km s}^{-1}$ , for runs with molecular cooling and having different abundance profiles.

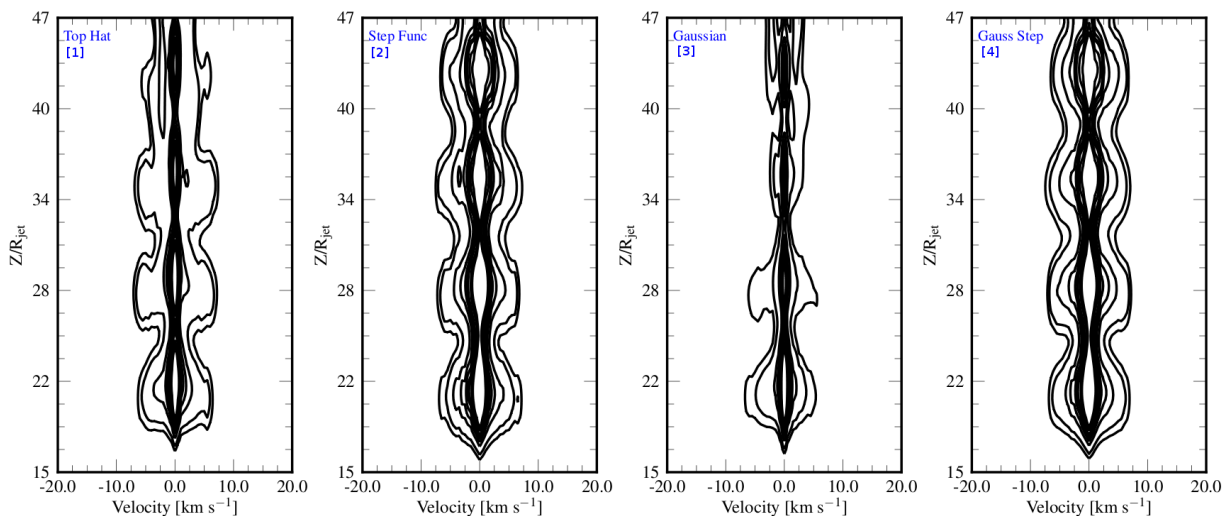


**Figure 11.** Position-velocity maps of SiO(2-1) for the internal knots produced in the model with reference parameters and different abundance profiles. The contours mark different levels of emission in K, viz., 0.1, 0.2, 0.6, 1.0, 1.4, 1.8, 2.0, 3.0, 4.0.

run. The left panel shows the integrated emission (as map and contours) of SiO(2-1), (5-4) and (8-7) lines, while the right panel shows the PV diagram for the same lines. The contour levels are marked on the color bar of each panel.

ALMA Cycle 0 observations have recently reported complex kinematic features of young bipolar molecular outflows. In particular, [Arce et al. \(2013\)](#) observed morphology, kinematics and entrainment of the HH 46/47 molecular outflow from a low mass nearby source ( $d = 450$  pc) using CO(1-0). They find that the red lobe of the outflow exhibits a very complex structure with a collimated episodic wind, whereas the outflow in the blue lobe is consistent with a wide-angle wind model. Three major clumps in the red lobe along the outflow axis appear as *wedges* in the PV diagram

(similar to that seen in the right panel of fig 12). A quantitative comparison is not possible due to the different molecule observed. Another source which is studied in details, with ALMA band 7 is one of the most energetic, luminous molecular outflows G331.512-0.103 ([Merello et al. 2013](#)). Observations of this outflow associated with a high-mass star reveal a compact, extremely young bipolar outflow and a symmetric out-flowing shell. Further, their PV diagrams with SiO and  $\text{H}^{13}\text{CO}^+$  show a characteristic peak at  $-45 \text{ km s}^{-1}$  along the primary axis that could be associated with a molecular *bullet* of high-velocity dense material as also found in our synthetic maps at inclination angles of  $60^\circ$  and  $45^\circ$ .

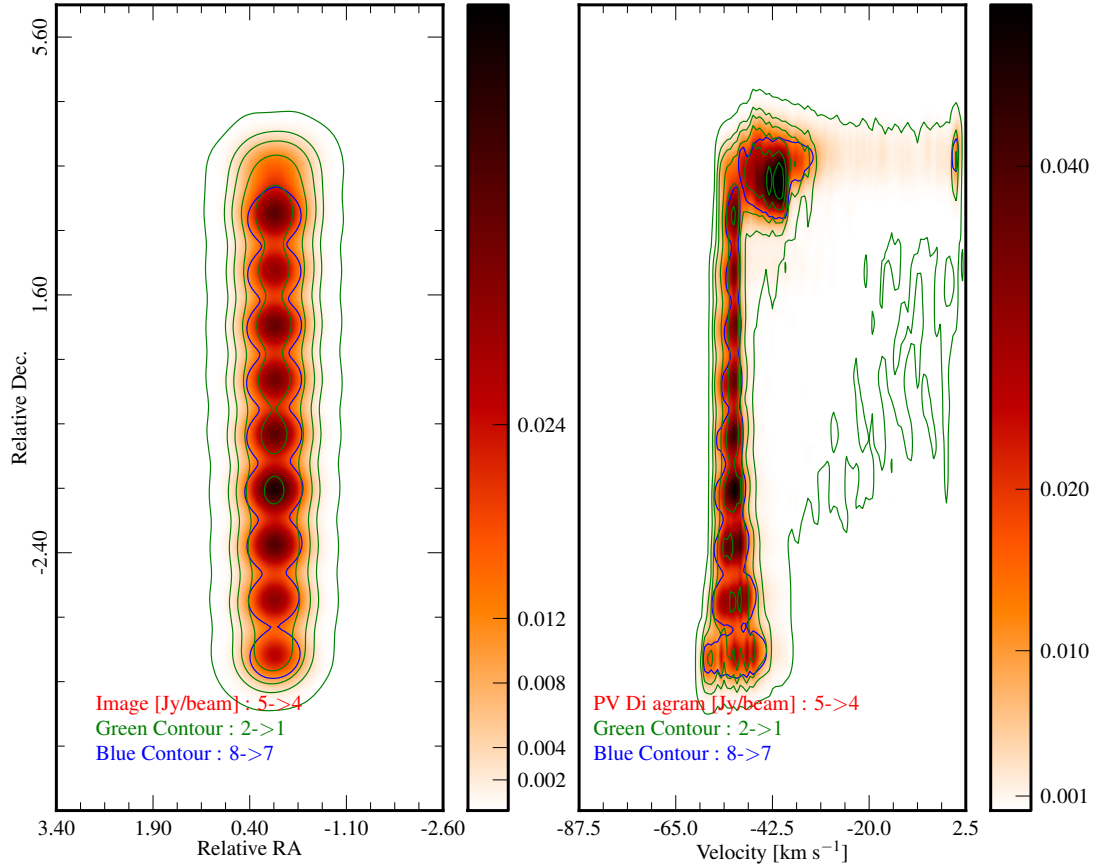


**Figure 12.** **Left:** The integrated intensity map of SiO(2-1), (5-4) and (8-7). The emission map shows the J=5-4 line intensity (in units of  $\text{Jy km s}^{-1}/\text{beam}$ ), the blue contours show the J=8-7 line intensity and the green contours show the J=2-1 line intensity. The jet is inclined at an angle of  $60^\circ$ . **Right:** The PV diagram taken along the axis of the jet for the 5-4 line (in units of  $\text{Jy/beam}$ ), showing the higher J transitions highlighting the knots of the jet and broad emission at the bow shock. In both panels the ticks on the color bar represent the different contour levels.

## 8 DISCUSSION

Here we compare our results with SiO observations of young low mass and high mass outflows.

### 8.1 EHV component and Molecular bullets

Multi-line mm-wavelength surveys of SiO emission towards a sample of molecular outflows have shown that these outflows exhibit both low and high velocity SiO emission possibly arising from two distinct regimes. The slow component in the case of a typical outflow, L1448, is believed to arise from the shell of accelerated ambient gas with SiO abundance lower by two orders of magnitude than regions emitting the high velocity component (Codella, Bachiller & Reipurth (1999)). In addition, an interesting feature of EHV gas is seen in many young molecular outflows. The origin of the EHV component is still a mystery, however, recent high resolution observations show that EHV gas is seen in

high density gas tracers (like CO and SiO) and the line have intensities  $\sim 0.1$  K (Tafalla et al. 2010).

In IRAS 04166+2706, Santiago-García et al. (2009) have shown that the EHV CO(2-1) emission is mapping a jet-like feature that consists of a collection of discrete peaks symmetrically placed on both outflow lobes. This symmetry indicate that such EHV peaks might arise from events that took place near the central source and have since propagated in the flow (Bachiller et al. 1990; Tafalla & Bachiller 2011). The dynamical model in conjunction with proper radiative transfer calculations presented here agrees very well with the above scenario. The *bullets* in our work are injected into the flow in a sinusoidal manner along with a collimated atomic jet. These pulsating ejections do interact with the medium via shocks and exciting high velocity gas. Including the cooling associated with molecules and the  $\text{H}_2$  chemistry allows us to consistently identify the regions where molecular hydrogen is formed and disassociated (see fig. 7). The SiO emission that we obtain from our radiative transfer calculations is associated with regions slightly behind where the



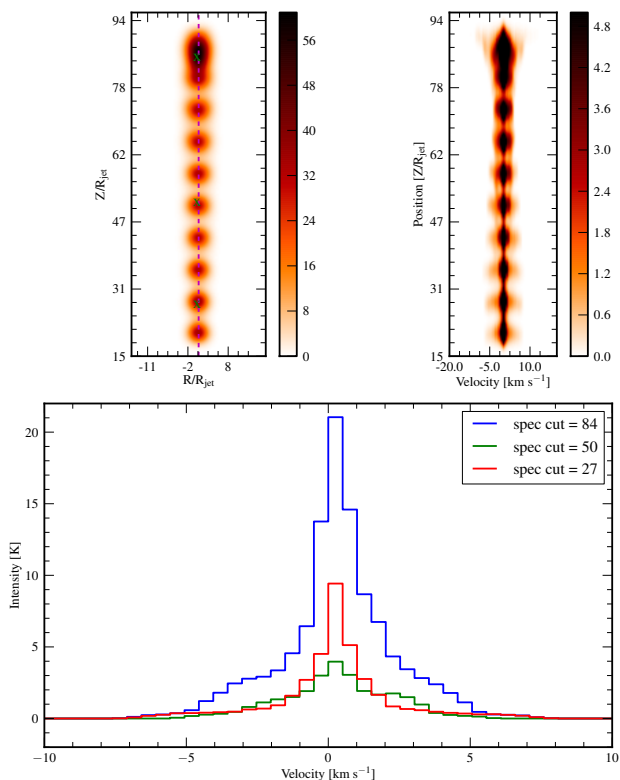


**Figure 8.** Integrated emission map (*top left*) in units of K-km s<sup>-1</sup>, PV diagram (*top right* in units of K and spectra (*bottom*) for the SiO(2-1) transition for the reference run. The jet is assumed to be in the plane of sky implying an angle of inclination of 90°. The vertical *magenta dashed* line represents the cut for the PV diagram and *green crosses* marks the positions from which the spectra are taken.

shocked H<sub>2</sub> gas is present as observed in case of L1157 molecular outflow *Gueth, Guilloteau & Bachiller (1998)*. A contour map of SiO emission obtained from the reference run is shown in figure 13. Further, we find SiO emission coming from velocities of the order of 40-70 km s<sup>-1</sup>, when  $i = 45^\circ$  (see fig 9). Additionally, we see a distinct saw-tooth pattern in the PV diagrams from our models (see figs. 9 and 12). These predictions from our model very well resembles the characteristic features of EHV SiO emission seen in the majority of the outflows (*Santiago-García et al. 2009; Tafalla & Bachiller 2011; Arce et al. 2013*).

All of the above striking similarities from observations of EHV gas and synthetic spectra and PV diagrams gives a very formidable backing to the idea that such an emission could arise due to shock interactions of internal knots in the flow.

## 8.2 Line transitions and ratio

Numerous molecular outflows with jet-like SiO bullets have been observationally studied till date. In particular, H7-11 (*Bachiller et al. 1998*), IRAS 04166+2706 (*Santiago-García et al. 2009; Tafalla et al. 2010*), HH211 (*Nisini et al. 2002*) L1448 (*Bachiller, Martín-Pintado & Fuente 1991; Nisini et al. 2007; Tafalla et al. 2010*) and L1157 (*Nisini et al. 2007*) have shown clear signatures of the EHV component. Among

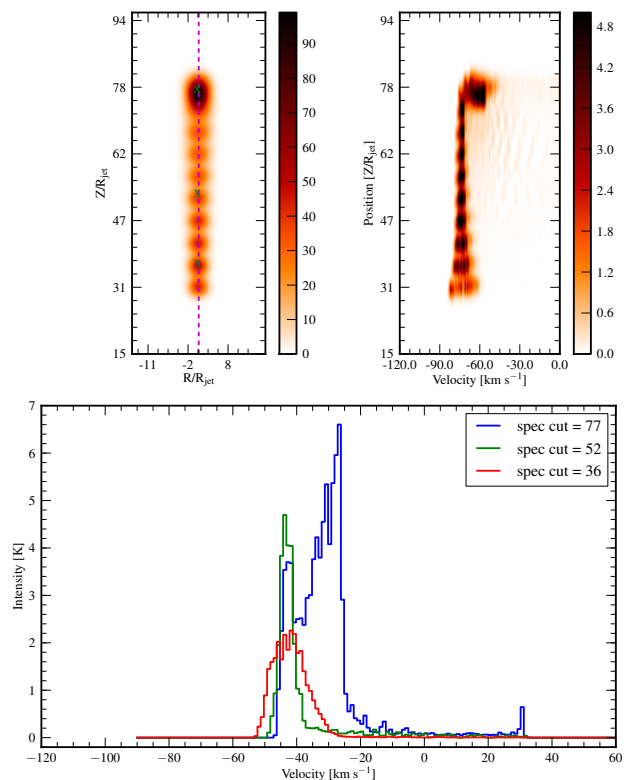


**Figure 9.** Same as figure 8 but with angle of inclination of 45°.

them, L1448, HH211 and L1157 have been studied in detail using an extensive multi-line survey of SiO. Such a multi-frequency analysis helps to understand the dependence of excitation conditions for these lines on velocity, based on existing shock models.

The most striking feature seen in the figure 13 is the progressive shift of emitting region from the interface to internal knots with increase in excitation energies of different lines. In particular, the lowest transition SiO(1-0) shows most of the emission coming from the interface between the jet and ambient medium, along with emission from the dense knots formed at the base of the flow. On the other hand, SiO(5-4) and (8-7) emission, is more concentrated in the inner jet regions and arise mainly from the shocks due to internal knots. Such a trend in emission with excitation energies coming from different SiO line transitions have been observed in young outflows (for L1448 bullets (*Nisini et al. 2007*), HH211 (*Chandler & Richer 2001; Nisini et al. 2002; Hirano et al. 2006*)). Further, the evolved post-shock gas near the bow shock also shows bright emission for these high J transitions. This gas is linked to the thermal instability associated with radiative jets (see section 6.1). The sub-structure seen close to the bow shock with high resolution does give a sense of clumpiness in the flow, backing the suggestions to explain clumpy SiO emission observed by *Chandler & Richer (2001)*.

*Nisini et al. (2007)* have shown that the current plane-parallel shock models fit reasonably well the physical conditions traced by the SiO emission i.e., temperature  $\lesssim 1000$  K and H<sub>2</sub> number density  $\sim 10^5$ - $10^6$  cm<sup>-3</sup>, assuming optically thin emission. They can also fit the observed fractional SiO

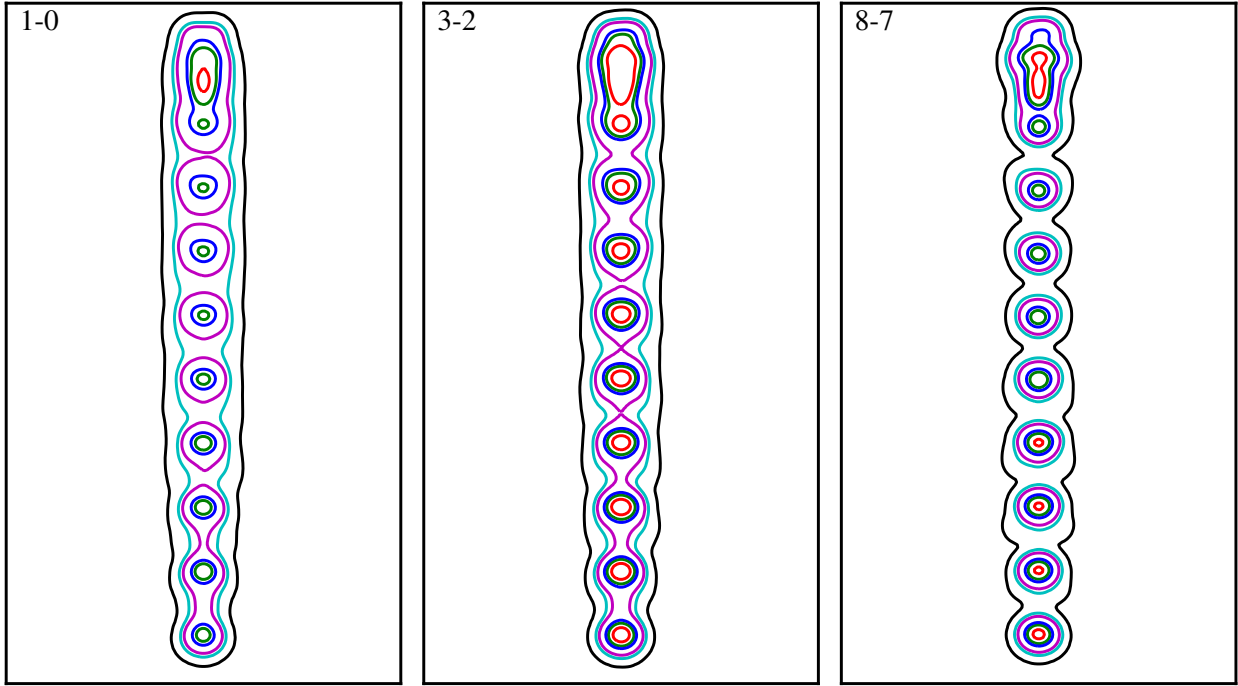


**Figure 13.** Contour maps of multi-line integrated SiO emission convolved with a  $2''$  beam obtained using parameters of the reference run. The line transitions are labelled on the top left corner of each panel. The contour colors represent different intensities in  $\text{K-km s}^{-1}$ , i.e. 50.0 (red), 30.0 (green), 20.0 (blue), 5.0 (magenta), 2.0 (cyan), 0.1 (black).

abundance of  $\sim 10^{-7}$  in these outflows. However, *they fail to predict all the line profiles and in particular their similarities for low and high excitation lines, which we are able to obtain.* Line emission for SiO from our model also traces similar physical environment. Fig. 7 shows that regions close to the internal knot have temperatures up to 1000 K and molecular hydrogen density of the order of  $10^6 \text{ cm}^{-3}$  (also see fig. 2). These are the regions where the bulk of the SiO emission is present, with fractional abundances between  $10^{-6}$  to  $10^{-8}$ . The line profiles shapes obtained from our study fit reasonably well that observed by Nisini et al. (2007), especially for the bullets seen in L1448. *Interestingly, in our models, the line profiles are equally broadened for low as well as high excitation lines.* The top panel of fig. 14 shows spectra for three line transitions for the reference run but with an angle of inclination  $i = 60^\circ$  and convolved with a single dish beam of  $15''$  to simulate observed integrated intensities of L1448 bullets observed with large beams from JCMT and IRAM. Intensities predicted from our reference model,  $\int T_{\text{MB}} dV = 5.76 \text{ K km s}^{-1}$  for SiO(2-1), lie within a factor of two from the observed values (Table 2 of Nisini et al. 2007).

The variation of normalized integrated single dish emission with upper transition levels  $J_{\text{up}}$  for the reference run is shown in the right panel of fig. 14. The curve obtained shows a distinct rise followed by a fall in integrated emission for higher transitions with a peak in emission for  $J_{\text{up}} = 3$ . Values  $\approx 1$  for line ratios SiO(8-7)/(5-4) and SiO(5-4)/(2-1)

have been found in HH212 (Cabrit et al. 2007; Lee et al. 2008) and also for molecular outflows from massive young stellar object in IRAS 17233-3606 (Leurini et al. 2013). The local velocity gradient (LVG) slab modeling with optically thin approximation were unable to produce these line ratios. In the present non-LTE radiative transfer modeling, no assumption of optical depths or photon escape probability are prescribed and line ratios are self consistently calculated and are shown in the bottom left panel of fig. 14. Their values lie very close to unity as indicated from observations. In summary, the shape, ratio and peak intensity of the spectra obtained from our model fit very well the observed values implying that SiO emission from our model is tracing regions with physical conditions similar to those observed.

### 8.3 Slow Component and Grain Chemistry

We have presented a simple model that is able to explain the spectral characteristics of the SiO EHV component seen in several young outflows. The reference model consistently solves for the  $\text{H}_2$  chemistry in the presence of appropriate cooling. The temperature, density and velocities obtained from dynamical simulation is used as input in the non-LTE radiative transfer code to obtain SiO maps, spectra and PV diagrams. One essential ingredient required for the radiative transfer modeling is the SiO fractional abundance and its dependence on shock velocity. Though 1D models that

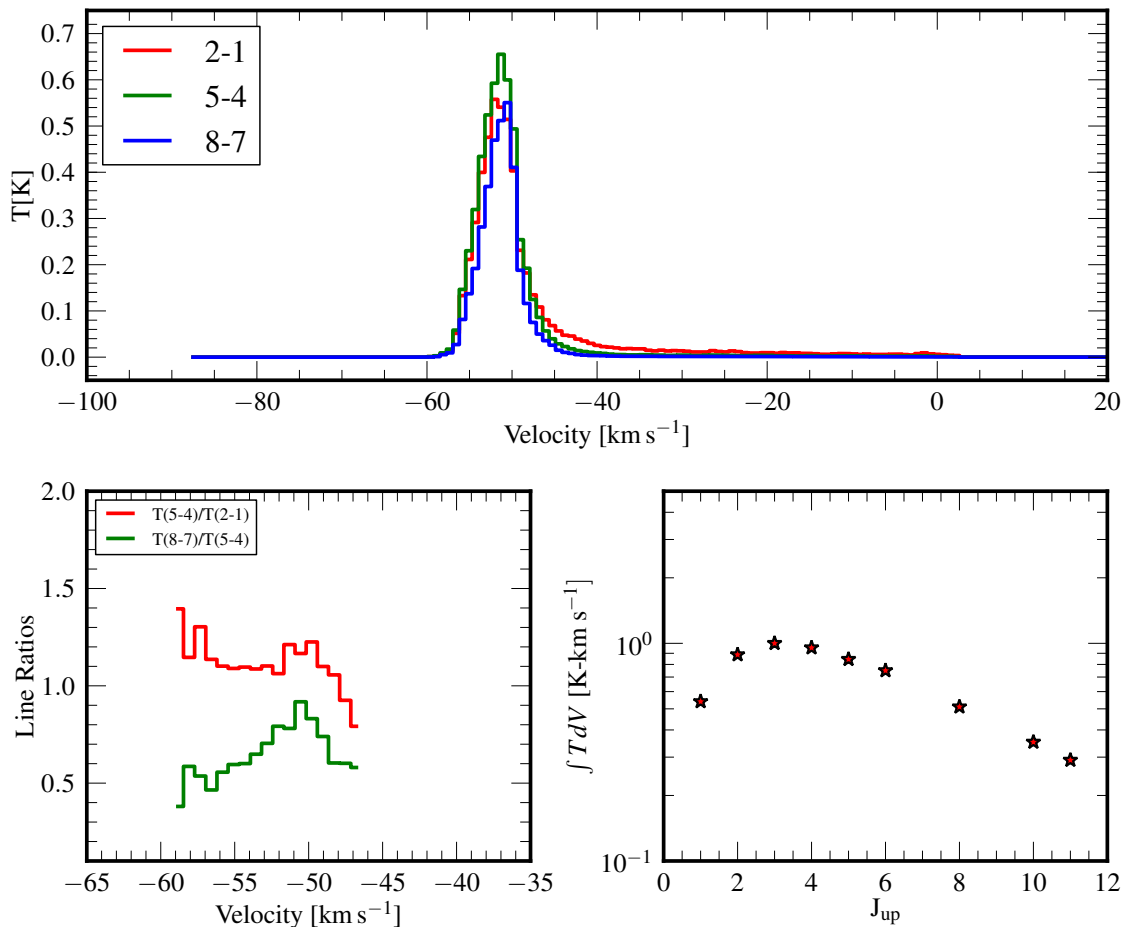


**Figure 14.** *Top:* Line profiles in SiO (2-1), (5-4) and (8-7) at one of the inner knots for the reference molecular cooling run. The profiles are obtained when the angle of inclination is 60° with respect to line of sight. *Bottom left:* Line intensity ratios SiO(8-7)/(5-4) and SiO(5-4)/(2-1), as a function of velocity. *Bottom right:* Variation of normalized integrated intensity with upper line transition  $J_{\text{up}}$  for the reference run.

study the formation of SiO in the gas phase from sputtering and grain-grain collisions exists, their focus is mainly on weaker C-type shocks (Schilke et al. 1997; Caselli, Hartquist & Havnes 1997; Gusdorf et al. 2008; Van Loo et al. 2013). The pulsating jet propagation model presented here have bulk velocities reaching up to 120 km s<sup>-1</sup>. We have used few simplified SiO abundance profiles as a function of jet velocity. Though the shape of the profile is uncertain, the upper and lower limits used are backed by observational evidences. Ideally, for a consistent dependence of SiO abundance on shock velocity, one would have to also solve for silicon and SiO chemistry in a manner similar to that of H<sub>2</sub>. However, such a numerically expensive model with complex chemistry is beyond the scope of this paper as this could imply to include grain processing and more gas-phase chemistry in an MHD multi-fluid approach.

The model presented in this paper targets the very early phases of molecular outflows i.e., dynamical time scales of ~ 1000 years. As discussed in sections above, the unique

combination of pulsating jet with simple chemistry and cooling followed by non-LTE radiative transfer calculations has shown success in fitting the line shapes, integrated intensity and line ratios of SiO transitions arising from EHV gas. However, the synthetic spectra show no signatures of slow SiO component that accompanies EHV emission seen in many outflows (e.g., Lefloch et al. 1998; Codella, Bachiller & Reipurth 1999). The physical mechanism for the origin of the slow SiO component is still a matter of debate. Codella, Bachiller & Reipurth (1999) suggest that it arises due to the slowing down of shocked gas as they age. The time scale estimated for the shocked gas to slow down is of the same order of magnitude as the SiO destruction time scale i.e., 10<sup>4</sup> years (Codella, Bachiller & Reipurth 1999). In this case, we do not expect to see the slow velocity SiO component, as our models stop at ~ 1000 yr. However, we do see initial hints of slowing down of more evolved gas in terms of the velocity shift of about 7-10 km s<sup>-1</sup> in peak emission between that coming from the freshly formed internal knots close to the

base of the flow and that from the more evolved gas near the bow shock. To ascertain this fact in more detail, one would need to track the bow shock for  $10^4$  years using a larger simulation box and possibly with adaptive gridding which will be considered for future simulations. Such a long term evolution will also help to provide a numerical model for the formation of HH objects which are believed to be slowed down and more evolved forms of our young molecular bullets, as suggested by Norman & Silk (1979) and Hartigan, Raymond & Hartmann (1987).

An alternative hypothesis for the origin of the low velocity SiO component is that it could be formed by interaction of wider slow shocks with the ambient medium. Generally it is assumed that the silicon material comes from dust grain cores and that it is necessary to sputter or vaporise such cores to obtain some SiO in gas phase. However, some silicon material may be mixed with the ices on the dust grain surfaces (see discussion in Schilke et al. 1997). In such a scenario, shocks with speeds below  $20 \text{ km s}^{-1}$  might inject a significant amount of silicon into the gas phase from the mantles, without completely destroying the grains. Jiménez-Serra et al. (2010) also found parsec-scale emission of SiO toward an infrared dark cloud, suggesting that large scale shocks (triggered by cloud-cloud collisions; Henshaw et al. 2013) may be responsible. Testing such scenarios is beyond the scope of the present model. One would not only need proper treatment of dust physics but also a two fluid model to study the impact of slow shocks in two dimensions. These models are indeed very important to study wide and slow emission from molecules like CO as seen in some young outflows like L1157 (Gómez-Ruiz et al. 2013) and  $\text{H}_2\text{O}$  as seen from recent results of the Herschel-WISH survey (Tafalla et al. 2013).

## 9 CONCLUSION

We have performed MHD simulations of episodic radiative jet propagating with a typical speed of  $100 \text{ km s}^{-1}$  into a cold, non-magnetized ambient molecular medium with a density gradient. The jet dynamical quantities are evolved in conjunction with different optically thin, non-equilibrium cooling prescriptions of varying complexities. The most complex is that of molecular cooling along with  $\text{H}_2$  chemistry. This prescription allows us to track the formation and destruction of HI, HII and  $\text{H}_2$  along with the flow dynamics. The final state of the jet obtained for each cooling model is then used as input into a non-LTE radiative transfer code to obtain SiO emission maps, spectra and PV digrams. The main results obtained from our study are as follows :

- Different cooling prescriptions used for our model significantly influence the thickness of the jet. An efficient mode of cooling does reduce the size of the cocoon and results in a more narrow jet. The bow shock structure differs with various cooling modes. With realistic cooling functions thermal instability develops at the jet head, which also shows a significant emission in SiO along with young internal knots that are formed close to the base of the jet.
- Emission maps obtained from our reference run with molecular cooling show a distinctive collimated outflow structure. The physical regions responsible of SiO emission in such early outflows typically have molecular hydrogen

densities  $n \sim 10^6 \text{ cm}^{-3}$  and temperatures  $> 500 \text{ K}$ , which is consistent with properties deduced from LVG modeling of observational data of young outflows like L1448-mm.

- Our multi-line study of SiO clearly shows how different line transitions are sensitive to different regions in the jets. For example, the SiO(1-0) transition is mostly excited due to the interaction of the jet with the ambient medium, while SiO(8-7) trace the inner most jet regions as they are excited only in the internal knots. This finding very well supports the multi-line observational surveys done for young molecular outflows, particularly, HH 211. Our models can also reproduce similarities in line profile shapes for low and high excitation lines.

- Single-dish synthetic spectra obtained from our model typically have intensities of 0.3-0.5 K, peak around  $50 \text{ km s}^{-1}$  and have a typical line width of  $20 \text{ km s}^{-1}$ . Such modeled spectra are in excellent agreement with characteristic features of EHV emission of SiO seen in young molecular outflows. The line ratios  $T(8-7)/T(5-4)$  and  $T(5-4)/T(2-1)$ , predicted from our models have values close to unity consistent with observations. Further, indications of the formation of the slow component due to the slowing down of the older knots is clearly seen as a shift of centroid velocities by  $7-10 \text{ km s}^{-1}$  at the end of the first  $10^3$  years of evolution.

- The predicted PV diagrams from our models show a distinctive saw-tooth features that are generally observed in outflows like IRAS 04166+2706.

- Emission from internal knots do depend on the chosen profile of the abundance. With the step profile all the internal knots emit SiO, whereas no emission is seen in knots when a Gaussian profile without a step is used. For the top-hat profile, we observe that emission mainly comes from knots close to the base of the flow and the condensation formed at the bow shock due to thermal instability.

- Predicted ALMA maps also show characteristic features that are consistent with young molecular outflows with EHV emission.

In summary, this work for the first time provides a simplified model that explains the origin of the EHV emission seen in SiO from the inner regions of young molecular outflows. The unique combination of axisymmetric jet propagation model with molecular cooling and non-LTE radiative transfer calculations can successfully reproduce most of the observed properties of SiO emission from young molecular outflows. This model provides an excellent template to compare current ALMA observations and can also predict signatures of thermal instabilities which can be tested with interferometric observations. In the future, we would like to extend our model to full three dimensions with adaptive mesh refinement and evolve the jet for longer time scales to explore slow velocity component, precession and other non-linear instabilities. Additionally, we would also like to have a better handle on SiO abundance, not only from observations but also by including dust micro-physics in our model.

## APPENDIX A: TREATMENT OF ADIABATIC INDEX $\gamma$

In dealing with a gas chemistry network which can have both monatomic and diatomic species, one is immediately



presented with the issue of how to treat the adiabatic index,  $\gamma$ , of the gas, which directly influences the equation of state, eq. 5, and thus the behavior of the gas. In standard hydrodynamical codes, the gas is generally assumed to be a monatomic ideal gas, with  $\gamma = 5/3$ . A diatomic gas, such as  $H_2$ , on the other hand, has a value of  $\gamma = 1.4$  at low temperatures, decreasing to below 1.3 at higher temperatures as the vibrational modes of the hydrogen molecule become excited. Thus, the value of  $\gamma$  for a gas containing a mixture of atomic and molecular hydrogen requires a temperature-dependent calculation of the  $\gamma$  value for  $H_2$  and a weighting of the values for the atomic and molecular components according to their abundance. Yoshida et al. (2006) have suggested a prescription of an effective  $\gamma$  which takes into account the corresponding weights of each chemical species and is given by,

$$\frac{1}{\gamma_{\text{eff}} - 1} = \frac{1}{\mu} \left[ \sum_i \frac{X_i}{A_i} \frac{1}{(\gamma_i - 1)} \right]^{-1}, \quad (\text{A1})$$

where  $i$  is the index for each specie and  $\mu$  is the mean molecular weight. The mass fraction is added in the above equation following the correction suggested in O'Sullivan & Camenzind (2009). Additionally, the temperature dependence in the case of  $H_2$  molecule can be obtained using Landau (1980),

$$\frac{1}{\gamma_{H_2} - 1} = \frac{1}{2} \left[ 5 + 2x^2 \frac{e^x}{(e^x - 1)^2} \right], \quad (\text{A2})$$

where the last term with  $x = 6100 \text{ K}/T$  accounts for the vibrational degree of freedom, with  $T$  being the gas temperature.

However, for such an implementation in large scale simulations, one must first consider its cost, effectiveness, and even correctness. Although such a method would indeed yield a more correct  $\gamma$  value for the gas mixture in conditions where the rotational and vibrational modes have had enough time to reach the level of excitation corresponding to the temperature of the gas, in cases where the gas has just been shocked, the method would produce an incorrect  $\gamma$  value. This is because the gas that passes through shock gets rapidly heated, but this energy goes predominantly into the translational degrees of freedom of the gas. It is only with time that energy goes into the rotational and vibrational degrees of freedom of the gas through collisions. Flower et al. (2003) states that the adiabatic index of the post-shock gas close to the ideal monatomic value of  $5/3$ , and that in order to calculate correctly its evolution as the gas relaxes one would have to model the rotational and vibrational levels of the hydrogen molecules in a time-dependent manner.

For the large-scale simulations present here it is more practical to use the standard value of  $5/3$  which is correct for the post-shock and predominantly atomic parts of the flow but incorrect for the equilibrated parts of the flow, with a significant fraction of molecular matter. As the shock regions and their effect on the molecular hydrogen content of the ambient gas are of primary importance here, we opt for the more relevant, and also simpler policy of keeping the normal  $\gamma$  value of  $5/3$  for our simulations.

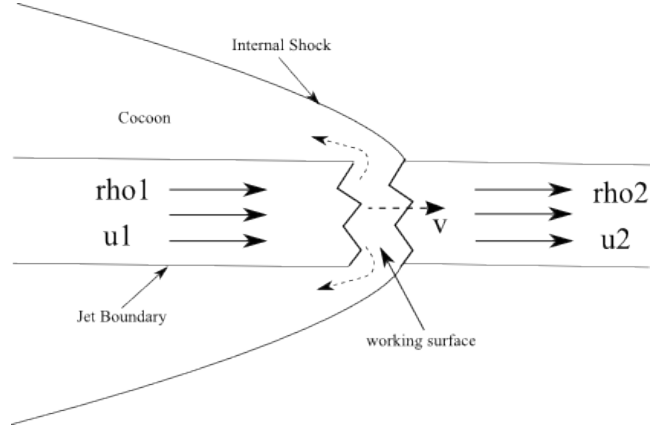


**Figure B1.** Schematic diagram showing the structure of the internal working surface. The faster upstream material with velocity  $u_1$  catches the slower downstream material with velocity  $u_2$  forming a two shock structure ( $u_1 > v > u_2$ ). The in-between gas is squeezed out sideways forming the cocoon.

## APPENDIX B: WORKING SURFACES AND SHOCKS

In this section we describe the mathematical derivation of estimating the speed of the working surface of the internal knot and shock speeds associated with it. We will follow the derivation as given in (Raga et al. 1990; Raga & Kofman 1992). Fig. B1 shows a cartoon representation of a single internal knot formed in the jet. The density and velocity upstream of the internal shock are  $\rho_1$  and  $u_1$ , while, the downstream values are  $\rho_2$  and  $u_2$  respectively. Note the velocities  $u_1$  and  $u_2$  are measured in a stationary frame of reference of the star. The velocity of the working surface is denoted by  $v$ , can be derived from the ram pressure balance between the upstream and downstream flow,

$$\rho_1(u_1 - v)^2 = \rho_2(v - u_2)^2. \quad (\text{B1})$$

This gives us the expression for  $v$  as,

$$v = \frac{u_1 + \zeta u_2}{1 + \zeta}, \quad (\text{B2})$$

where,

$$\zeta = \sqrt{\frac{\rho_2}{\rho_1}}.$$

The parameter  $\zeta$  is obtained in principle from the two dimensional snapshot of the jet density. In case of bow shock, the downstream medium is the stationary ambient medium ( $u_2 = 0$ ), thus, eq. B2 will reduce to eq. 8. However for the internal knots, the variation of density and velocity for the reference run is shown in fig. B2. The value of  $\zeta$  is about 1 for most of the internal knots seen in our simulations. Thus, the velocity of the working surface simplifies to,

$$v = \frac{u_1 + u_2}{2}. \quad (\text{B3})$$

Additionally, the shock velocity (i.e, the velocity of the pre-shock flow with respect to the velocity of the working surface) of the upstream and downstream facing shocks have the same velocity given by Raga et al. (1990):

$$w = \frac{u_1 - u_2}{2} = 0.5\Delta u. \quad (\text{B4})$$

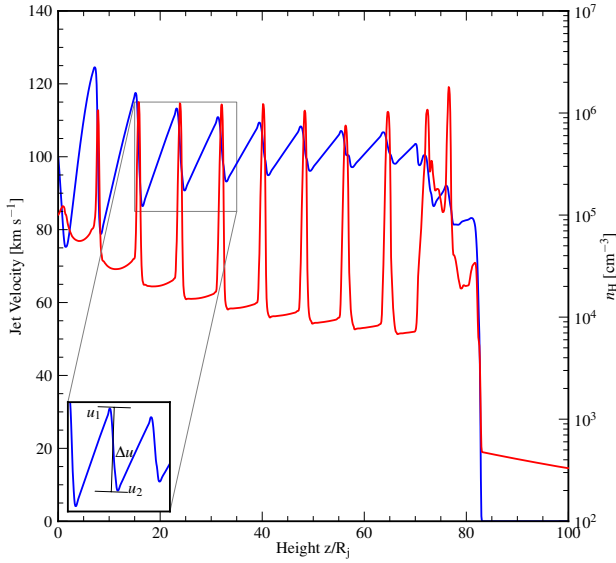


**Figure B2.** Variation of jet velocity (blue) and density (red) as a function of height close to the axis of the flow. The inset on the bottom left of the figure shows a zoomed variation of velocity and clearly marks the peak to peak difference between the upstream and downstream components.

The difference in the pre- and post-discontinuity velocities,  $\Delta u$ , is marked clearly in fig. B2. Typically, the difference in velocity values for our reference runs lie around 15–40 km s<sup>−1</sup>. Thus, the shock velocity  $w$  lies around 10–20 km s<sup>−1</sup>. Similar values are also obtained for jets like HH 34 by [Raga & Kofman \(1992\)](#).

## REFERENCES

- Abel T., Anninos P., Zhang Y., Norman M. L., 1997, *New A*, 2, 181
- Arce H. G., Goodman A. A., 2001a, *ApJ*, 554, 132
- Arce H. G., Goodman A. A., 2001b, *ApJ*, 551, L171
- Arce H. G., Mardones D., Corder S. A., Garay G., Noriega-Crespo A., Raga A. C., 2013, *ApJ*, 774, 39
- Arce H. G., Shepherd D., Gueth F., Lee C.-F., Bachiller R., Rosen A., Beuther H., 2007, *Protostars and Planets V*, 245
- Bacciotti F., Chiuderi C., Oliva E., 1995, *A&A*, 296, 185
- Bacciotti F., Ray T. P., Mundt R., Eislöffel J., Solf J., 2002, *ApJ*, 576, 222
- Bachiller R., 1996, *ARA&A*, 34, 111
- Bachiller R., Guilloteau S., Gueth F., Tafalla M., Dutrey A., Codella C., Castets A., 1998, *A&A*, 339, L49
- Bachiller R., Martin-Pintado J., Fuente A., 1991, *A&A*, 243, L21
- Bachiller R., Martin-Pintado J., Tafalla M., Cernicharo J., Lazareff B., 1990, *A&A*, 231, 174
- Bally J., 2007, *Ap&SS*, 311, 15
- Beuther H., Schilke P., Sridharan T. K., Menten K. M., Walmsley C. M., Wyrowski F., 2002, *A&A*, 383, 892
- Blandford R. D., Payne D. G., 1982, *MNRAS*, 199, 883
- Blondin J. M., Fryxell B. A., Konigl A., 1990, *ApJ*, 360, 370
- Brinch C., Hogerheijde M. R., 2010, *A&A*, 523, A25
- Cabrit S., Bertout C., 1992, *A&A*, 261, 274
- Cabrit S., Codella C., Gueth F., Nisini B., Gusdorf A., Dougados C., Bacciotti F., 2007, *A&A*, 468, L29
- Canto J., Raga A. C., 1991, *ApJ*, 372, 646
- Caselli P., Hartquist T. W., Havnes O., 1997, *A&A*, 322, 296
- Caselli P. et al., 2012, *ApJ*, 759, L37
- Cen R., 1992, *ApJS*, 78, 341
- Cerqueira A. H., de Gouveia dal Pino E. M., 1999, *ApJ*, 510, 828
- Chandler C. J., Richer J. S., 2001, *ApJ*, 555, 139
- Codella C., Bachiller R., Reipurth B., 1999, *A&A*, 343, 585
- Crapci A., Caselli P., Walmsley C. M., Myers P. C., Tafalla M., Lee C. W., Bourke T. L., 2005, *ApJ*, 619, 379
- Dionatos O., Nisini B., Cabrit S., Kristensen L., Pineau Des Forêts G., 2010, *A&A*, 521, A7
- Dionatos O., Nisini B., Garcia Lopez R., Giannini T., Davis C. J., Smith M. D., Ray T. P., DeLuca M., 2009, *ApJ*, 692, 1
- Dougados C., Bacciotti F., Cabrit S., Nisini B., 2010, in *Lecture Notes in Physics*, Berlin Springer Verlag, Vol. 793, Lecture Notes in Physics, Berlin Springer Verlag, Garcia P. J. V., Ferreira J. M., eds., p. 213
- Downes T. P., Cabrit S., 2003, *A&A*, 403, 135
- Downes T. P., Cabrit S., 2007, *A&A*, 471, 873
- Dutrey A., Guilloteau S., Bachiller R., 1997, *A&A*, 325, 758
- Flower D. R., Le Boulrot J., Pineau des Forêts G., Cabrit S., 2003, *MNRAS*, 341, 70
- Galli D., Palla F., 1998, *A&A*, 335, 403
- Glassgold A. E., Mamon G. A., Huggins P. J., 1991, *ApJ*, 373, 254
- Goddi C., Greenhill L. J., Chandler C. J., Humphreys E. M. L., Matthews L. D., Gray M. D., 2009, *ApJ*, 698, 1165
- Gómez-Ruiz A. I., Hirano N., Leurini S., Liu S.-Y., 2013, *ArXiv e-prints*
- Gueth F., Guilloteau S., 1999, *A&A*, 343, 571
- Gueth F., Guilloteau S., Bachiller R., 1998, *A&A*, 333, 287
- Guillet V., Jones A. P., Pineau Des Forêts G., 2009, *A&A*, 497, 145
- Gusdorf A., Cabrit S., Flower D. R., Pineau Des Forêts G., 2008, *A&A*, 482, 809
- Hartigan P., Frank A., Varnière P., Blackman E. G., 2007, *ApJ*, 661, 910
- Hartigan P., Raymond J., Hartmann L., 1987, *ApJ*, 316, 323
- Henshaw J. D., Caselli P., Fontani F., Jiménez-Serra I., Tan J. C., Hernandez A. K., 2013, *MNRAS*, 428, 3425
- Hirano N., Liu S.-Y., Shang H., Ho P. T. P., Huang H.-C., Kuan Y.-J., McCaughrean M. J., Zhang Q., 2006, *ApJ*, 636, L141
- Hollenbach D., McKee C. F., 1979, *ApJS*, 41, 555
- Jiménez-Serra I., Caselli P., Tan J. C., Hernandez A. K., Fontani F., Butler M. J., van Loo S., 2010, *MNRAS*, 406, 187
- Keto E., Caselli P., 2010, *MNRAS*, 402, 1625
- Konigl A., Pudritz R. E., 2000, *Protostars and Planets IV*, 759

- Landau L. D., 1980, Statistical physics : part 1. Butterworth-Heinemann, Oxford
- Lee C.-F., Ho P. T. P., Bourke T. L., Hirano N., Shang H., Zhang Q., 2008, *ApJ*, 685, 1026
- Lefloch B., Castets A., Cernicharo J., Loinard L., 1998, *ApJ*, 504, L109
- Leurini S., Codella C., Gusdorf A., Zapata L., Gómez-Ruiz A., Testi L., Pillai T., 2013, *A&A*, 554, A35
- Lloyd S., 1982, Information Theory, *IEEE Transactions on*, 28, 129
- Martin-Pintado J., Bachiller R., Fuente A., 1992, *A&A*, 254, 315
- Masson C. R., Chernin L. M., 1992, *ApJ*, 387, L47
- Masson C. R., Chernin L. M., 1993, *ApJ*, 414, 230
- Merello M., Bronfman L., Garay G., Lo N., Evans, II N. J., Nyman L.-Å., Cortés J. R., Cunningham M. R., 2013, *ApJ*, 774, L7
- Mignone A., Bodo G., Massaglia S., Matsakos T., Tesileanu O., Zanni C., Ferrari A., 2007, *ApJS*, 170, 228
- Morse J. A., Heathcote S., Hartigan P., Cecil G., 1993, *AJ*, 106, 1139
- Mundt R., Brugel E. W., Buehrke T., 1987, *ApJ*, 319, 275
- Neufeld D. A., Dalgarno A., 1989a, *ApJ*, 340, 869
- Neufeld D. A., Dalgarno A., 1989b, *ApJ*, 344, 251
- Nisini B., Codella C., Giannini T., Richer J. S., 2002, *A&A*, 395, L25
- Nisini B., Codella C., Giannini T., Santiago Garcia J., Richer J. S., Bachiller R., Tafalla M., 2007, *A&A*, 462, 163
- Norman C., Silk J., 1979, *ApJ*, 228, 197
- Offner S. S. R., Arce H. G., 2013, *ArXiv e-prints*
- Offner S. S. R., Lee E. J., Goodman A. A., Arce H., 2011, *ApJ*, 743, 91
- O’Sullivan J., Camenzind M., 2009, Molecular Cooling in Large Scale Simulations of Protostellar Jets, Tsinganos K., Ray T., Stute M., eds., pp. 453–458
- Panoglou D., Cabrit S., Pineau Des Forêts G., Garcia P. J. V., Ferreira J., Casse F., 2012, *A&A*, 538, A2
- Podio L., Bacciotti F., Nisini B., Eisloffel J., Massi F., Giannini T., Ray T. P., 2006, *A&A*, 456, 189
- Powell K. G., Roe P. L., Linde T. J., Gombosi T. I., de Zeeuw D. L., 1999, *Journal of Computational Physics*, 154, 284
- Raga A., Cabrit S., 1993, *A&A*, 278, 267
- Raga A. C., Binette L., Canto J., Calvet N., 1990, *ApJ*, 364, 601
- Raga A. C., Kofman L., 1992, *ApJ*, 386, 222
- Raga A. C., Taylor S. D., Cabrit S., Biro S., 1995, *A&A*, 296, 833
- Rathborne J. M., Simon R., Jackson J. M., 2007, *ApJ*, 662, 1082
- Rawlings J. M. C., Redman M. P., Carolan P. B., 2013, *MNRAS*, 435, 289
- Ray T., 2012, in *EAS Publications Series*, Vol. 58, *EAS Publications Series*, pp. 105–112
- Ray T., Dougados C., Bacciotti F., Eisloffel J., Chrysostomou A., 2007, *Protostars and Planets V*, 231
- Santiago-García J., Tafalla M., Johnstone D., Bachiller R., 2009, *A&A*, 495, 169
- Schilke P., Walmsley C. M., Pineau des Forets G., Flower D. R., 1997, *A&A*, 321, 293
- Shang H., Allen A., Li Z.-Y., Liu C.-F., Chou M.-Y., Anderson J., 2006, *ApJ*, 649, 845
- Shu F. H., Ruden S. P., Lada C. J., Lizano S., 1991, *ApJ*, 370, L31
- Smith M. D., Rosen A., 2003, *MNRAS*, 339, 133
- Stone J. M., Hardee P. E., 2000, *ApJ*, 540, 192
- Tafalla M., Bachiller R., 2011, in *IAU Symposium*, Vol. 280, *IAU Symposium*, Cernicharo J., Bachiller R., eds., pp. 88–102
- Tafalla M. et al., 2013, *A&A*, 551, A116
- Tafalla M., Santiago-García J., Hacar A., Bachiller R., 2010, *A&A*, 522, A91
- Teşileanu O., Mignone A., Massaglia S., 2008, *A&A*, 488, 429
- Vaidya B., Fendt C., Beuther H., Porth O., 2011, *ApJ*, 742, 56
- Vaidya B., Goddi C., 2013, *MNRAS*, 429, L50
- Van Loo S., Ashmore I., Caselli P., Falle S. A. E. G., Hartquist T. W., 2013, *MNRAS*, 428, 381
- Woodall J., Agúndez M., Markwick-Kemper A. J., Millar T. J., 2007, *A&A*, 466, 1197
- Yoshida N., Omukai K., Hernquist L., Abel T., 2006, *ApJ*, 652, 6
- Ziurys L. M., Friberg P., Irvine W. M., 1989, *ApJ*, 343, 201